High resolution laboratory x-ray tomography for biomedical research

From design to application

Dreier, Till

2023

Document Version:
Publisher's PDF, also known as Version of record

High resolution laboratory x-ray tomography for biomedical research

From design to application

TILL DREIER
MEDICAL RADIATION PHYSICS, LUND | FACULTY OF SCIENCE | LUND UNIVERSITY

High resolution laboratory x-ray tomography for biomedical research

High resolution laboratory x-ray tomography for biomedical research

From design to application

Till Dreier

LUND UNIVERSITY

DOCTORAL DISSERTATION

Doctoral dissertation for the degree of Doctor of Philiosphy (PhD) at the Faculty of Science at Lund University to be publicly defended on Friday, the 12th of May 2023 at 09:00 at Lundmarksalen, Astronomihuset, Sölvegatan 27, 223 62 Lund.

Faculty opponent
Prof. Dr. Chris Jacobsen
Department of Physics and Astronomy, Northwestern University, Evanston, IL, USA
and Advanced Photon Source, Argonne National Laboratory, Argonne, IL, USA

Organization	Document name
LUND UNIVERSITY Department of Medical Radiation Physics Universitetssjukhuset, 221 85 Lund, Sweden	**DOCTORAL DISSERTATION** Date of disputation 2023-05-12 Sponsoring organization
Author(s) Till Dreier	

Title and subtitle

High resolution laboratory x-ray tomography for biomedical research: From design to application

Abstract

Laboratory x-ray micro- and nano-tomography are emerging techniques in biomedical research. Through the use of phase-contrast, sufficient contrast can be achieved in soft tissue to support medical studies. With ongoing developments of x-ray sources and detectors, biomedical studies can increasingly be performed at the laboratory and do not necessary require synchrotron radiation. Particularly nano-focus x-ray sources offer new possibilities for the study of soft tissue. However, with increasing resolution, the complexity and stability requirements on laboratory systems advance as well. This thesis describes the design and implementation of two systems: a micro-CT and a nano-CT, which are used for biomedical imaging.

To increase the resolution of the micro-CT, super-resolution imaging is adopted and evaluated for x-ray imaging, grating-based imaging and computed tomography utilising electromagnetic stepping of the x-ray source to acquire shifted low-resolution images to estimate a high-resolution image. The experiments have shown that super-resolution can significantly improve the resolution in 2D and 3D imaging, but also that upscaling during the reconstruction can be a viable approach in tomography, which does not require additional images.

Element-specific information can be obtained by using photon counting detectors with energy-discriminating thresholds. By performing a material decomposition, a dataset can be split into multiple different materials. Tissue contains a variety of elements with absorption edges in the range of 4 – 11 keV, which can be identified by placing energy thresholds just below and above these edges, as we have demonstrated using human atherosclerotic plaques.

An evaluation of radiopaque dyes as alternative contrast agent to identify vessels in lung tissue was performed using phase contrast micro-tomography. We showed that the dye solutions have a sufficiently low density to not cause any artefacts while still being able to separate them from the tissue and distinguish them from each other.

Finally, the design and implementation of the nano-CT system is discussed. The system performance is assessed in 2D and 3D, achieving sub-micron resolution and satisfactory tissue contrast through phase contrast. Application examples are presented using lung tissue, a mouse heart, and freeze dried leaves.

Key words

x-ray, computed tomography, micro-CT, nano-CT, phase contrast, biomedical, super-resolution, material decomposition

Classification system and/or index terms (if any)

Supplementary bibliographical information	Language
	English
ISSN and key title	ISBN
	978-91-8039-613-4 (print) 978-91-8039-614-1 (pdf)
Recipient's notes	Number of pages: 155 / Price
	Security classification

High resolution laboratory x-ray tomography for biomedical research

From design to application

Till Dreier

LUND
UNIVERSITY

Cover illustration front: 3D render of a mouse fetus scanned in the developed micro-CT.

Faculty of Science
Department of Medical Radiation Physics

ISBN: 978-91-8039-613-4 (print)
ISBN: 978-91-8039-614-1 (pdf)

Printed in Sweden by Media-Tryck, Lund University, Lund 2023

Media-Tryck is a Nordic Swan Ecolabel
certified provider of printed material.
Read more about our environmental
work at www.mediatryck.lu.se

MADE IN SWEDEN

Contents

Abstract

Laboratory x-ray micro- and nano-tomography are emerging techniques in biomedical research. Through the use of phase-contrast, sufficient contrast can be achieved in soft tissue to support medical studies. With ongoing developments of x-ray sources and detectors, biomedical studies can increasingly be performed at the laboratory and do not necessary require synchrotron radiation. Particularly nano-focus x-ray sources offer new possibilities for the study of soft tissue. However, with increasing resolution, the complexity and stability requirements on laboratory systems advance as well. This thesis describes the design and implementation of two systems: a micro-CT and a nano-CT, which are used for biomedical imaging.

To increase the resolution of the micro-CT, super-resolution imaging is adopted and evaluated for x-ray imaging, grating-based imaging and computed tomography utilising electromagnetic stepping of the x-ray source to acquire shifted low-resolution images to estimate a high-resolution image. The experiments have shown that super-resolution can significantly improve the resolution in 2D and 3D imaging, but also that upscaling during the reconstruction can be a viable approach in tomography, which does not require additional images.

Element-specific information can be obtained by using photon counting detectors with energy-discriminating thresholds. By performing a material decomposition, a dataset can be split into multiple different materials. Tissue contains a variety of elements with absorption edges in the range of 4 – 11 keV, which can be identified by placing energy thresholds just below and above these edges, as we have demonstrated using human atherosclerotic plaques.

An evaluation of radiopaque dyes as alternative contrast agent to identify vessels in lung tissue was performed using phase contrast micro-tomography. We showed that the dye solutions have a sufficiently low density to not cause any artefacts while still being able to separate them from the tissue and distinguish them from each other.

Finally, the design and implementation of the nano-CT system is discussed. The system performance is assessed in 2D and 3D, achieving sub-micron resolution and satisfactory tissue contrast through phase contrast. Application examples are presented using lung tissue, a mouse heart, and freeze dried leaves.

Sammanfattning

Laboratoriebaserad röntgenmikro- och nano-tomografi är framväxande tekniker inom biomedicinsk forskning. Användning av faskontrast möjliggör tillräcklig kontrast i vävnadsprov för att stödja medicinska studier. Med den pågående utvecklingen av röntgenkällor och detektorer, kan allt fler biomedicinska studier utföras i laboratoriet i stället för på en synkrotronljusanläggning. Nano-fokuserade röntgenkällor erbjuder särskilt nya möjligheter för studier av vävnadsprov, men med ökande upplösning ökar komplexiteten och stabilitetskraven blir striktare. Denna avhandling beskriver design och implementering av två system: en mikro-CT och en nano-CT, som används för biomedicinsk avbildning.

För att öka upplösningen i våra mikro-CT används superupplösningsavbildning och detta utvärderas för röntgenavbildning, tomografi samt gitter-baserad avbildning. Elektromagnetisk stegning av röntgenkällan används för att erhålla förskjutna lågupplösta bilder som sedan kombineras för att skapa en högupplöst bild. Experimenten visade att superupplösning kan förbättra upplösningen avsevärt i 2D- och 3D-bilder, men också att uppskalning under rekonstruktionen kan vara ett alternativ inom tomografi, vilket inte kräver ytterligare bilder.

Elementspecifik information kan erhållas genom att använda fotonräknande detektorer med energidiskriminerande trösklar. Materialnedbrytning gör det möjligt att identifiera olika element i provet. Vävnad innehåller en mängd olika element med absorptionskanter i området från 4 – 11 keV, som kan identifieras genom att placera energitrösklar precis under och ovanför dessa kanter. Vi visade konceptet med hjälp av mänskliga aterosklerotiska plack.

En utvärdering av färgämnen som alternativt kontrastmedel för att identifiera kärl i lungvävnad gjordes med faskontrastmikrotomografi. Vi visade att färglösningarna har en tillräckligt låg densitet för att inte orsaka artefakter samtidigt som de går att särskilja från vävnaden och varandra.

Slutligen diskuteras design och implementering av nano-CT systemet. Systemets prestanda utvärderas i 2D och 3D, med resultat som visar att submikrometerupplösning och tillräcklig vävnadskontrast uppnås genom användandet av faskontrast. Avbildningsresultat för lungvävnad, mushjärta, och frystorkade löv presenteras som exempel på tillämpningar.

List of publications

This thesis is based on the following publications, referred to by their Roman numerals:

I **Super-resolution X-ray imaging with hybrid pixel detectors using electromagnetic source stepping**
T. Dreier, U. Lundström, M. Bech
Journal of Instrumentation 15(3) C03002 (2020)
doi: 10.1088/1748-0221/15/03/C03002

II **Super-resolution X-ray phase-contrast and dark-field imaging with a single 2D grating and electromagnetic source stepping**
K. R. Rix‡, **T. Dreier**‡, T. Shen, M. Bech
Physics in Medicine and Biology 64(16) 165009 (2019)
doi: 10.1088/1361-6560/ab2ff5

III **Improved resolution in x-ray tomography by super-resolution**

T. Dreier, N. Peruzzi, U. Lundström, M. Bech
Applied Optics 60(20) 5783 – 5794 (2021)
doi: 10.1364/AO.427934

IV **Material decomposition in low-energy micro-CT using a dual-threshold photon counting x-ray detector**
R. Solem, **T. Dreier**, I. Goncalves, M. Bech
Frontiers in Physics 9:673843 (2021)
doi: 10.3389/fphy.2021.673843

V **Radiopaque dyes allow vessel imaging in lung tissue using laboratory phase contrast micro-CT**
T. Dreier, G. Bernström, S. Ganji, C. Norvik, K. Tran-Lundmark, M. Bech
Proceedings of SPIE, Developments in X-Ray Tomography XIV, 12242 (2022)
doi: 10.1117/12.2632343

VI **Laboratory x-ray nano-computed tomography for biomedical research**

T. Dreier, R. Krüger, M. Bech
Unpublished manuscript (2023)

‡ Shared first author

List of contributions

The authors contributions to the included publications:

I I designed and carried out the experiments, performed the analysis, developed processing scripts, and performed the CT reconstruction using a freely available software. I wrote the manuscript and am the first author of the paper.

II This project was taken over from from K. Rix, who had previously worked on a proof of concept. I rebuilt the imaging setup and implemented repeatable x-ray source stepping. Data processing was moved from a freely available toolbox to custom processing scripts to extract absorption, dark-field, and differential phase contrast images from the measurements and to create super-resolution images. The manuscript was re-written by me based on an initial draft from K. Rix. I am shared first author of the paper.

III The experiments were designed, carried out, and analysed by me after implementing new detectors into the micro-CT setup. A CT reconstruction pipeline was implemented together with N. Peruzzi. I wrote the manuscript and am the first author.

IV The study was proposed by me and I assisted in the technical implementation and data analysis. I was a supervisor of the first author and assisted in the writing of the manuscript.

V I contributed to the design of the study and was the main responsible for the data acquisition, processing, and reconstruction. Together with the co-authors, I was involved in the analysis and interpretation of the data. I wrote the manuscript and am the first author.

VI The presented nano-CT system was designed and implemented by me. I developed the acquisition, processing, and reconstruction pipelines and performed the presented experiments. I wrote the manuscript and am the first author.

Publications not included in this thesis

The author has contributed to the following publications, which are relevant to this thesis, but have not been included:

α **Sub-micrometer morphology of human atherosclerotic plaque revealed by synchrotron radiation-based μCT—A comparison with histology**
M. Truong[‡], **T. Dreier**[‡], J. Wassélius, L. Sundius, A. Persson, G. Lovric, A. Bonnin, I. Goncalves, M. Bech
PLoS ONE 17(4):e0265598 (2022)
doi: 10.1371/journal.pone.0265598

β **Shunt-type plexiform lesions identified in the Sugen5416/hypoxia rat model of pulmonary arterial hypertension using synchrotron-based phase-contrast micro-CT**
O. van der Have, C. Westöö, F. Ahrné, X. Tian, K. Ichimura, **T. Dreier**, C. Norvik, M. E. Kumar, E. Spiekerkoetter, K. Tran-Lundmark
European Respiratory Journal 59(6):2102802 (2022)
doi: 10.1183/13993003.02802-2021

γ **X-ray in-line holography and holotomography at the NanoMAX beamline**
S. Kalbfleisch, Y. Zhang, M. Kahnt, K. Buakor, M. Langer, **T. Dreier**, H. Dierks, P. Stjärneblad, E. Larsson, K. Gordeyeva, L. Chayanun, D. Söderberg, J. Wallentin, M. Bech, P. Villanueva-Perez
Journal of Synchrotron Radiation 29(1) 224 – 229 (2022)
doi: 10.1107/S1600577521012200

δ **Dose-efficient multimodal microscopy of human tissue at a hard X-ray nanoprobe beamline**
S. Sala, Y. Zhang, N. De La Rosa, **T. Dreier**, M. Kahnt, M. Langer, L. B. Dahlin, M. Bech, P. Villanueva-Perez, S. Kalbfleisch
Journal of Synchrotron Radiation 29(3) 1 – 9 (2022)
doi: 10.1107/S1600577522001874

ϵ **Optimization of phase contrast imaging with a nanofocus X-ray tube**

H. Dierks, **T. Dreier**, R. Krüger, M. Bech, J. Wallentin
Unpublished manuscript (2023)

ζ **eSoil: Low power bioelectronic growth scaffold enhances crop biomass via electrical stimulation**
V. K. Oikonomou, M. Huerta, **T. Dreier**, Y. Daguerre, A. Sandéhn, M. Berggren, E. Pavlopoulou, T. Näsholm, M. Bech, E. Stavrinidou
Manuscript in review (2023)

η **Tuning structural and mechanical properties of cellulose based conducting scaffolds**
V. K. Oikonomou‡, **T. Dreier**‡, J. L. Christensen, A. B. Dahl, V. A. Dahl, M. Bech, E. Stavrinidou
Unpublished manuscript (2023)

θ **Capillary organic electronic ion pump enables in-vivo biomolecule delivery in succulent plants and elucidating their effect on stomatal signaling**
A. Sandéhn, I. Bernacka-Wojcik, C. Routier, **T. Dreier**, O. Hodek, T. Moritz, M. Bech, D. Cowan-Turner, E. Stavrinidou
Unpublished manuscript (2023)

ι **Clustering methods for the characterization of synchrotron radiation X-ray fluorescence images of human carotid atherosclerotic plaque**
N. De La Rosa, N. Peruzzi, **T. Dreier**, M. Truong, U. Johansson, S. Kalbfleisch, I. Goncalves, M. Bech
Unpublished manuscript (2023)

‡ Shared first author

1 Introduction

With the discovery of x-rays by Röntgen (1898) in 1895, it became possible to image internal structures of opaque objects that could not be penetrated by visible light. Röntgen famously demonstrated this by taking an image of his wife's hand. Shortly after Röntgen's discovery, the potential use of x-rays in medicine was realised [Frost (1896)] and developed into what is referred to as radiography today, a standard diagnostic method in medicine. A famous early application were the radiography units headed by Marie Curie during the first world war, where x-rays were used to find foreign objects inside the bodies of wounded soldiers. During the early years, adverse health effects were reported with several pioneers losing limbs or dying as consequence of their radiation exposure leading to the first international organisation for the protection against ionising radiation [EANM (2016)].

With the development of digital imaging sensors in the 1960s [Boyle and Smith (1970)] and computers becoming more powerful, x-ray Computed Tomography (CT) was first implemented by Hounsfield (1973) in the 1970s. With CT, 3-dimensional images of the internal structure of objects can be obtained by performing a reconstruction on many radiography images acquired at different angles. While it took until the 1970s for CT to become technically feasible, its mathematical foundation had been described in 1914 by Radon (1986). Nowadays, CT is an invaluable diagnostic technique in medical imaging with continuous development and improvement, most recently the introduction of photon counting detectors [Taguchi and Iwanczyk (2013); Gomes and Manakkal (2022)].

Developments at synchrotron light sources, introduced in the 1970s, have lead to the advancement of fields like x-ray microscopy [Jacobsen (2019)] with spatial resolutions down to the diffraction limit of x-rays at a few nm [Thibault et al. (2008); Pfeiffer (2018)] and the utilisation of alternative contrast mechanisms, like phase contrast imaging [Snigirev et al. (1995); Cloetens et al. (1999); Paganin et al. (2002)]. With advances in x-ray tube and detector technologies, higher resolutions became available for laboratory use. X-ray micro-CT, as compared to clinical CT with resolutions of ≥ 0.5 mm, has become a common tool in medical research, material science, non-destructive testing, and industrial inspection. High-brightness sources [Hemberg et al. (2003); Tuohimaa et al. (2007)] are a key development to improve image quality in challenging applications like soft tissue imaging [Larsson et al. (2011, 2016); Töpperwien et al. (2017); Vågberg et al. (2018); Peruzzi et al. (2020); Quenot et al. (2022)], where phase contrast imaging is commonly used, in grating- or speckle-based imaging, where exposure times are typically very long [Bech et al. (2013); Zhou et al. (2015)], or in imaging of dynamic processes [Kim et al. (2017); Vavřík et al. (2017)]. Recently, nano-CT systems are finding increasing use in biomedical research [Müller et al. (2017); Ferstl et al. (2018); Romell et al. (2021); Eckermann et al. (2020)] and material science [Nachtrab et al. (2014); Fella et al. (2018); Graetz et al. (2021); Müller et al. (2021, 2022)].

Phase contrast is arguably one of the most important techniques in modern high-resolution biomedical x-ray imaging [Gureyev et al. (2009); Bravin et al. (2013)]. While soft tissue is typically considered to be too weakly absorbing for conventional CT, phase contrast exploits the refractive index as an alternative contrast mechanism. Phase contrast was first discovered by Zernike (1942) using visible light and later pioneered for x-rays using gratings by Bonse and Hart (1965). In the 1990s, the idea was adopted for biomedical imaging by Momose and Fukuda (1995); Momose et al. (1996) using a Talbot-Lau grating interferometer. Around the same time, a new method to achieve phase contrast was developed at the European Synchrotron Radiation Facility (ESRF) in Grenoble, France by Snigirev et al. (1995) utilising free space propagation, instead of gratings, based on the work on visible light holography by Gabor (1948) in the late 1940s. Propagation-based and Grating-based x-ray imaging were later adopted from synchrotron to laboratory sources by Wilkins et al. (1996); Pfeiffer et al. (2006). Currently, grating-based imaging is reaching clinical imaging in mammography [Stampanoni et al. (2011)] and lung imaging [Willer et al. (2021); Viermetz et al. (2022)].

This thesis deals with the development of laboratory micro- and nano-CT systems for biomedical imaging. In combination with the micro-CT system, method development was performed on super-resolution, particularly by using electromagnetic source stepping, for 2D imaging, single-grating imaging, and tomography. Further, material decomposition was implemented using an energy-discriminating detector to decompose tissue into different materials via absorption edges of naturally occurring elements. Phase contrast imaging was performed on paraffin embedded lung tissue in an evaluation study of radiopaque dye solutions as method to identify and track vessels. Then, a nano-CT system was built and verified for high-resolution tomography of biomedical objects using propagation-based phase contrast. In additional manuscripts and papers, not included in this thesis, further applications of propagation-based phase contrast tomography are discussed for both systems. With the systems developed and characterised as well as processing and reconstruction pipelines implemented, further developments and applications to the field of biomedical imaging are possible in the future.

The following chapter briefly introduces the background on x-rays, their interaction with matter, generation using laboratory sources, and detection with imaging detectors. Then the main concepts of x-ray imaging, computed tomography and its reconstruction, resolution, and image quality are described. In Chapter 3, the design and implementation, of the micro- and nano-CT systems built during this thesis, are described. Chapter 4 describes applications of the CT systems from super-resolution to energy-resolved imaging to imaging of soft tissue as a summary of the Papers I – V and experiments related to the nano-CT system described in Paper VI. Finally, Chapter 5 concludes the thesis.

2 Theory

2.1 X-ray fundamentals

X-rays are electromagnetic radiation, like e.g. visible light and microwaves, with much higher photon energies and short wavelengths as illustrated in Figure 2.1. Due to these properties, x-rays can penetrate objects and, in principle, allow for much higher resolution than visible light, which in practice is not achieved due to technical limitations. In imaging, the photon energy is defining the interaction of x-rays with different materials. Photon energy is measured in electron volt (eV), equivalent to the energy of an electron accelerated by a potential of 1 V, approximately 1.6×10^{-19} J. The main photon energies used in this thesis are in the range of 4 - 30 keV, utilising x-ray sources with acceleration voltages of up to 70 kV. The maximum photon energy produced by a 70 kV source is 70 keV, however, lower energies contribute significantly more to the contrast in low density biomedical objects and the used detectors are significantly more efficient at lower energies.

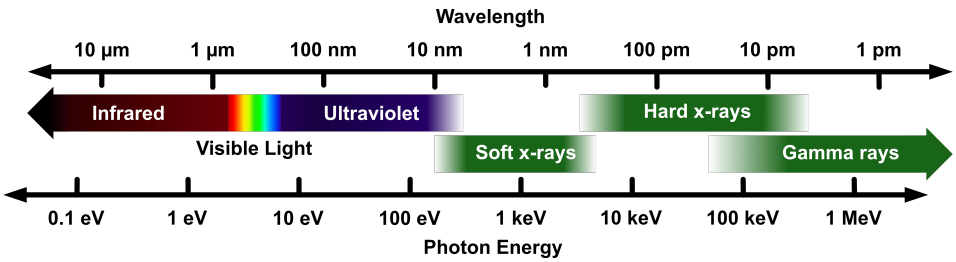

Figure 2.1: Sketch of the electromagnetic spectrum.

2.2 X-ray interaction with matter

X-rays moving through an object are attenuated by the different materials present in the object. Attenuation depends on the thickness z and attenuation coefficient μ as described by the Beer-Lambert law [Beer (1852); Mayerhöfer et al. (2020)]:

$$I = I_0 e^{-\mu z}, \tag{2.1}$$

where I is the resulting intensity of transmitted x-rays through the object and I_0 is the intensity of the x-ray beam before passing through the object. The attenuation coefficient μ for photon energies used in biomedical imaging consists mainly of two effects: photoelectric absorption and Compton scattering, as shown in Figure 2.2. At lower energies, most interactions are due to photoelectric absorption, while Compton scattering contributes more to the attenuation coefficient with increasing energy. Additionally, coherent scattering occurs as well, where x-rays are scattered without transferring energy to the electron during the interaction. Thus, coherently scattered photons retain their energy and change direction.

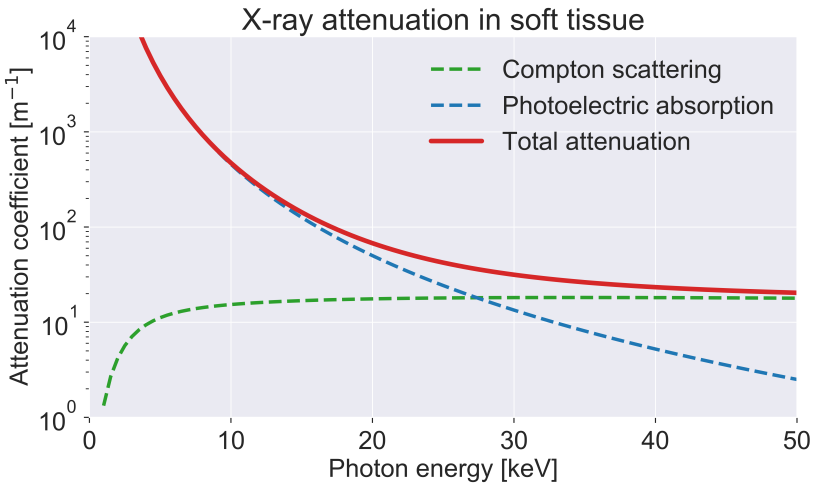

Figure 2.2: Attenuation coefficient of soft tissue comprised of contributions from photoelectric absorption and Compton scattering. *Data from NIST XCOM [Berger et al. (1998)]*

The majority of interactions of low energy x-ray photons are attributed to the photoelectric effect, where a photon, with an energy of at least the binding energy of the encountered electron, is absorbed and transfers all of its energy to the electron. This causes ionisation of the atom leading to the ejection of a photoelectron from the atom. The atom is left in an elevated state and needs to fill the vacancy left in its electron structure. When filling the vacancy, the excess energy leaves the atom either by emission of an Auger electron or emission of a characteristic x-ray. Auger emission describes the phenomenon when a loosely bound electron is emitted from the atom, carrying away the excess energy. Characteristic emission, also called fluorescence, results in the emission of an x-ray photon from the atom with specific element dependant energies, e.g. an electron transition from the L shell to the K shell of the atom causes the emission of a K_α photon, which has a specific energy for a given atom [Podgoršak (2009)]. Fluorescence becomes more likely with increasing atomic number Z [Attwood and Sakdinawatt (2017)], thus the Auger effect is dominant at low energies.

With increasing energy, Compton scattering becomes the predominant cause of attenuation, as shown in Figure 2.2, and has an almost negligible dependence on energy and Z. Compton scattering is inelastic (incoherent) scattering, i.e. the photon transfers a fraction of its energy to the electron and changes direction with the scattering electron departing at a different angle, carrying away the excess energy. The amount of energy transferred depends on the scattering angle. At lower photon energies, typically only a small fraction of energy is transferred [Attix (2008)]. In contrast, elastic (coherent) scattering, where no energy transfer takes place upon interaction, does not contribute to the attenuation, but rather the phase shift.

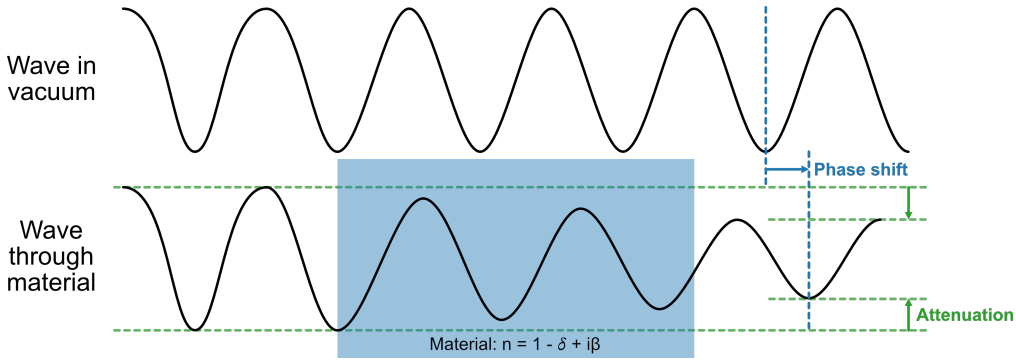

Figure 2.3: Attenuation and phase shift experienced by a wave passing through a material.

Photons propagating through a medium also experience a phase shift, determined by the complex refractive index n of the material traversed:

$$n = 1 - \delta + i\beta \tag{2.2}$$

where δ is responsible for the phase shift and the imaginary β for the attenuation [Attwood and Sakdinawatt (2017)]. δ is proportional to ρ_e/E^2, where ρ_e is the electron density and E is the photon energy. β is described through the total attenuation μ: $\beta = \frac{\lambda}{4\pi}E$, where λ is the photon wavelength. The detailed mathematical background and application to x-rays is described by Mayo et al. (2002). Considering hard x-rays, the effect of phase shifts for low density materials, like soft tissue, are much more significant than the effect on the attenuation [Schulz et al. (2010)]. To illustrate the effect of the refractive index, the x-rays are described as a plane wave propagating through a material, as shown in Figure 2.3.

2.3 X-ray production by laboratory sources

Modern laboratory x-ray sources utilise the same principle as the tubes used by Röntgen when he discovered x-rays [Röntgen (1898)]. While significant technical development has taken place improving resolution and flux, such as rotating anode and MetalJet sources [Hemberg et al. (2003)], the basic principle has not changed. Much higher flux and resolution can be achieved at large-scale facilities, such as synchrotrons and free-electron lasers, which use accelerators to generate x-rays. Such facilities are mainly used in research due to their high cost. All papers included in this thesis utilise laboratory sources.

Laboratory x-ray sources produce x-rays using a metal anode, often referred to as target. To generate x-rays, an electron beam is accelerated and focused on the target. Upon impact, the metal target produces an x-ray spectrum consisting of characteristic emission and bremsstrahlung as described in Chapter 2.2 and depicted in Figure 2.4 . Bremsstrahlung is produced through deceleration of electrons in the electric field of the atomic nucleus in the target. During deceleration, the electron loses energy, which is

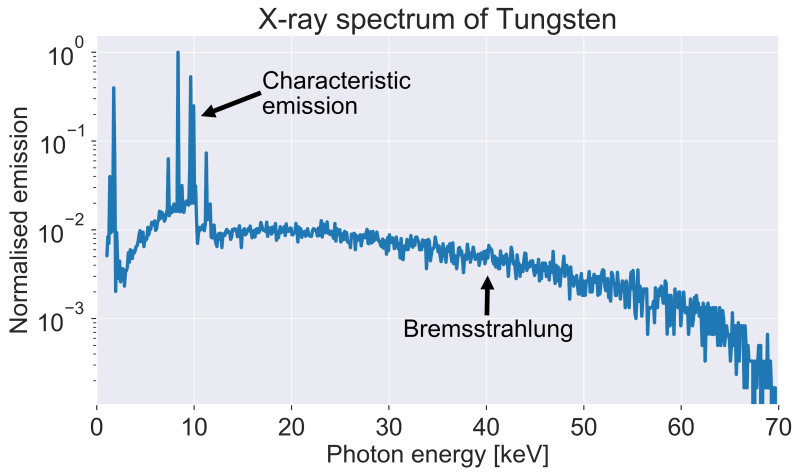

Figure 2.4: X-ray emission spectrum from a Tungsten target at an acceleration voltage of 70 kV. Simulation by Daniel Larsson, Excillum AB.

emitted as an x-ray photon [Podgoršak (2009)]. Bremsstrahlung produces a continuous x-ray spectrum, where the upper limit is set by the acceleration voltage as described in Chapter 2.1. Materials with a higher atomic number Z and a higher acceleration voltages make bremsstrahlung generation more likely [Bushberg et al. (2013)].

Important parameters of a source for imaging applications are: the main energy and maximum energy defined by the target material and acceleration voltage respectively, the size of the x-ray spot, and the flux, i.e. the amount of photons emitted from the source. The target material is often a compromise between characteristic energy, efficiency to generate x-rays, and thermal loading capacity. Managing the thermal load is particularly important since about 99 % of the energy of the electron beam is converted into heat. Generally, the aim is to generate as many x-rays as possible in a spot that is as small as possible with an energy range that gives good contrast for the targeted application without damaging the x-ray target. Damage to the target results in a loss of flux and deformation of the x-ray spot, i.e. loss of resolution. Typical target materials are Copper (Cu), Silver (Ag), Molybdenum (Mo), and Tungsten (W). These materials may be used as bulk target, embedded into Cu or diamond for improved heat conductivity, or as thin layer on a diamond window, especially for high-resolution transmission sources shown in Figure 2.5B. MetalJet sources utilises Gallium (Ga) and Indium (In) alloys as target material, which are liquid close to room temperature..

Laboratory x-ray sources can be split into two basic types: reflection and transmission tubes as shown in Figure 2.5. Reflection tubes use larger targets that allow for higher thermal loading through heat dissipation in a larger volume. A common approach to increase the power in reflection tubes is a line focus, i.e. the target is placed at a shallower angle and the width of the electron beam is increased. This distributes the heat generation

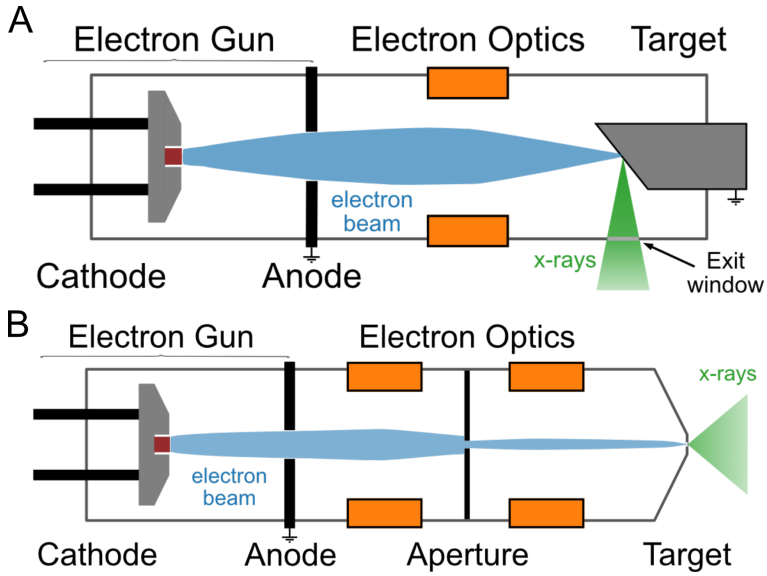

Figure 2.5: Sketches of x-ray sources showing the principal components: an electron gun consisting of a heated cathode emitting electrons with high voltage applied and a grounded anode hole, electron optics to focus and position the accelerated electron beam, and metal target used to generate x-rays. **(A)** Reflection type x-ray source commonly used for micro-focus tubes. **(B)** Transmission type x-ray source commonly used for nano-focus tubes.

over a larger area on the target, while the observed x-ray spot still appears round. Other approaches to increase the thermal loading capacity are rotating anode tubes, where the target continuously rotates, or the MetalJet source, where the target is a fast moving jet of liquid metal moving the heat away [Hemberg et al. (2003)]. Reflection tubes are available with x-ray spot sizes down to about 5 µm.

To achieve smaller x-ray spots, transmission tubes are used [Nachtrab et al. (2014)]. Their main difference compared to reflection tubes is that the x-ray spot is generated in a thin metal layer on a diamond window. The diamond window seals the tube while also acting as a heat conductor. This allows to place objects much closer to the source for higher geometric magnification. Further, transmission tubes can achieve significantly smaller x-ray spots down to a few hundred nm.

2.4 X-ray imaging detectors

Detectors used in x-ray imaging generally consist of a 2-dimensional array of pixels, like regular cameras. Relevant parameters to consider are the physical pixel size, the Point-Spread Function (PSF), and the detection quantum efficiency. The PSF describes how a detector responds to incoming photons, i.e. over how many pixels the signal is distributed. An acquired image can be described as a convolution of the object with the PSF. The detection quantum efficiency describes how efficiently different photon energies

are detected. Commonly, two different types of detectors are in use in research, industry, and medicine: scintillator-based detectors and photon counting detectors.

The most common type in imaging are scintillator-based detectors as shown in Figure 2.6A. These detectors are based on the Charged Coupled Device (CCD), the first digital imaging sensor presented by Boyle and Smith (1970). Modern detectors utilise a Scientific Complementary Metal-Oxide Semiconductor (sCMOS) chip based on the same principle. These detector chips are sensitive to photons with a wavelength in, or close to, the visible spectrum (see Figure 2.1). Thus, incoming x-ray photons have to be converted to be detected using a scintillator screen, i.e. a material that emits visible light photons when exposed to x-rays. This can be achieved with a simple phosphor screen, however, materials commonly in use today are Gadolinium Oxisulfide (Gadox), Caesium Iodine (CsI), or Lutetium Aluminium Garnet (LuAG).

Choice of scintillator material and thickness have a significant influence on the quantum efficiency and achievable resolution of the detector. Further reduction in detection efficiency occur in the coupling of the scintillator to the detector chip, e.g. in a fibre-optic plate, and the quantum efficiency of the detector chip itself has to be considered as well. A significant advantage of scintillator-based detectors is the ability to incorporate visible light optics to achieve magnification in the camera improving the resolution [Koch et al. (1998)]. It should also be noted that scintillator-based detectors exhibit thermal and readout noise, which typically are accounted for by correction with dark-field images, i.e. acquisitions without any x-rays present. In research, high-resolution sCMOS cameras are commonly used with pixel sizes down to 5 µm, typically thinner scintillators, and sometimes optics. So called FlatPanel detectors, on the other hand, are very common in industrial and medical imaging offering large areas and high efficiency at higher energies through thicker scintillators and larger pixels, often $\geq$ 100 µm.

Photon counting detectors were developed at CERN in the late 1990s [Campbell et al. (1998)] and detect x-ray photons directly using a semiconductor sensor in which photons create a charge cloud of electron-hole pairs upon interaction. Each pixel is comprised of dedicated electronics, which are bump-bonded to the sensor as depicted in Figure 2.6B. Energy-discriminating thresholds are incorporated into the pixels, which are used to suppress noise and obtain energy information, as discussed in Chapter 2.5.4 [Rossi et al. (2006); Williams et al. (2013); Krapohl (2015); Jowitt et al. (2022)]. A major advantage of these detectors is a much better PSF, often assumed to be a single pixel. While there is no interaction between the electronics, charge sharing between pixels can occur through diffusion of the generated charge cloud in the sensor, emission of a fluorescence photon, or simply a photon being detected at the border between pixels [Rossi et al. (2006)].

The quantum efficiency depends on the sensor material, typically Silicon (Si), Gallium Arsenide (GaAs), or Cadmium Telluride (CdTe). Si is almost 100 % efficient at 10 keV, but quickly drops with increasing energy [Donath et al. (2013)]. In combination with the very low noise, photon counting detectors are particularly well suited for imaging of low contrast

objects [Flenner et al. (2023)]. Applications requiring higher energies utilise CdTe, which cannot be produced in the same quality as Si and is not stable over time. As in intermediate material GaAs can be used providing very high efficiency up to about 50 keV mitigating some of the issues with CdTe [Fröjdh et al. (2011); Maneuski et al. (2012); Dudak and Zemlicka (2022)]. GaAs has also shown promise in biomedical imaging as demonstrated by Scholz et al. (2020).

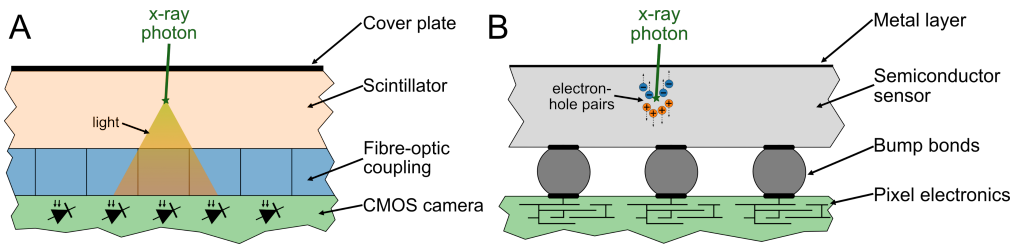

Figure 2.6: Sketches of **(A)** a scintillator-based detector consisting of a scintillator coupled to a CMOS camera via a fibre-optic plate and **(B)** a photon counting detector consisting of a semiconductor sensor bump bonded to individual pixel electronics.

2.5 X-ray imaging

2.5.1 Absorption and phase contrast

In common x-ray imaging techniques used in industry and medicine, contrast is achieved through the difference in attenuation of x-rays passing through an object consisting of different elements, as described by the Beer-Lambert law (Equation 2.1). Hence, the measured intensity will be lower after passing through a denser or thicker part of an object as shown in Figure 2.7A.

Small or low-density objects, such as soft tissue, absorb very little x-rays and thus yield low contrast making it difficult to impossible to resolve or distinguish features inside the object. Phase contrast offers an alternative contrast mechanism utilising phase shifts caused by the complex refractive index n (Equation 2.2) of different materials, as described in Chapter 2.2. The phase cannot be measured directly, but can be turned into measurable intensity variations [Snigirev et al. (1995)].

A common way to utilise phase shifts is Propagation-based Phase Contrast Imaging (PB-PCI) as described by Snigirev et al. (1995); Wilkins et al. (1996) and shown in Figure 2.7B. The distance between the object and detector is increased so detectable intensity variations can form, which are then visible on a high-resolution detector. This yields a compound image containing absorption and phase contrast. A phase retrieval algorithm is applied to translate the detected intensity variations into a contrast enhancement [Snigirev et al. (1995)]. Common algorithms are e.g. the single-material algorithm developed by Paganin et al. (2002) or Bronnikov Aided Correction (BAC) [De Witte et al. (2009a,b)]. These single-distance algorithms perform a deconvolution with an estimated filter kernel,

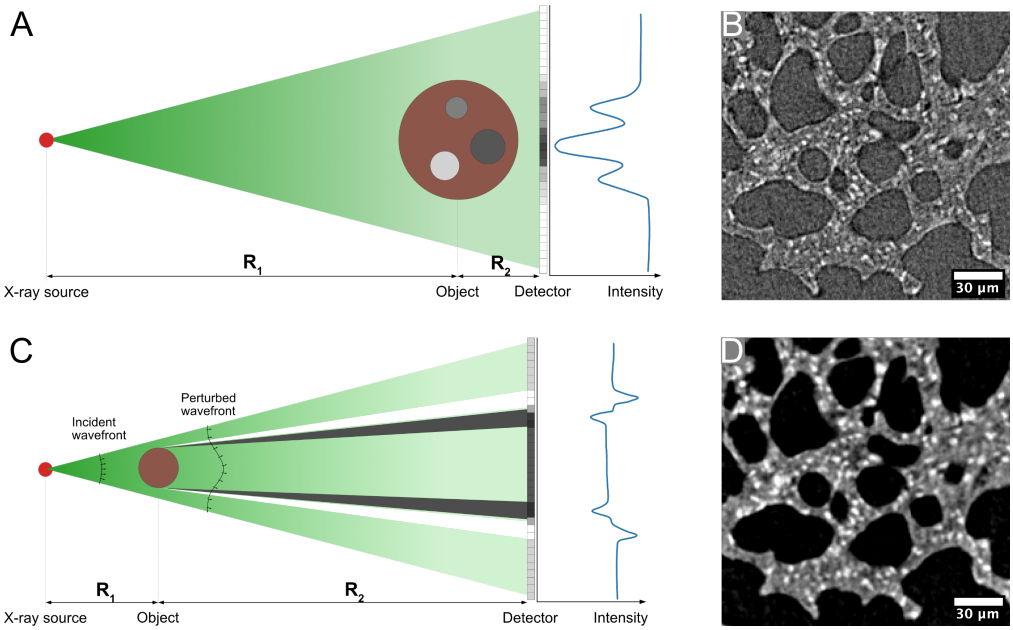

Figure 2.7: Principles of absorption contrast and phase contrast imaging with an example using a CT scan of paraffin embedded mouse lung tissue. **(A)** Conventional absorption-based x-ray imaging using a x-ray cone beam. **(B)** Reconstructed slice with absorption contrast. **(C)** Propagation-based phase contrast imaging where the object causes a phase shift of the incident x-rays, which are turned into measurable intensity variations by letting the perturbed wavefront propagate to the detector. **(D)** Reconstructed slice with phase-retrieval applied. *Sample provided by Olof Gidlöf, Lund University.*

which typically adds blur to the image reducing the resolution. To recover part of the lost resolution, an unsharp mask can be added as described by Sheppard et al. (2004); Paganin et al. (2020). An overview of different algorithms is provided by Burvall et al. (2011, 2013).

There are a variety of approaches to obtain phase contrast using optical elements, gratings, or diffusers. Most notable is the Talbot interferometer, developed for x-rays by Momose and Fukuda (1995); Momose et al. (2003); Weitkamp et al. (2005); Pfeiffer et al. (2006), utilising a phase grating to cause a phase shift and an analyser grating to resolve the phase fringes on the detector. This approach allows to extract complementary modalities from the images, shown in Figure 2.8: differential phase shifts and scattering, often referred to as dark-field. In recent years, dark-field imaging has been a valuable technique in a variety of applications, from imaging of fibres [Hannesschläger et al. (2015)] or porous materials [Blykers et al. (2021)] to medical applications in lung imaging, from initial developments described by Pfeiffer et al. (2008, 2013); Tapfer et al. (2011, 2012); Yaroshenko et al. (2013) to clinical applications described by Willer et al. (2021); Viermetz et al. (2022).

A variety of similar methods have been developed, often with the goal to simplify the setup. Approaches like single-shot imaging developed byWen et al. (2010), which is used in

Figure 2.8: Absorption, differential phase, and dark-field modalities extracted from a radiography of a mouse using a grating interferometer. *Figure adapted from Bech et al. (2013).*

Paper III, edge illumination [Olivo and Speller (2007)], and Talbot illuminators [Gustschin et al. (2021)] find increasing use. Speckle-based imaging [Morgan et al. (2012)] has been developed to work with a diffuser, such as sand paper, instead of a grating, which also led to the development of Unified Modulation Pattern Analysis (UMPA) [Zdora et al. (2017)], a versatile algorithm to extract dark-field and phase contrast modalities.

2.5.2 Resolution, contrast, and noise

Spatial resolution, often just referred to as resolution, describes the smallest features an imaging system can reliably detect. The achievable resolution is influenced by a variety of parameters, most importantly: pixel size and PSF of the detector, size of the x-ray spot, but also the contrast of the object. There is also a difference between resolving and being able to quantify features. To perform measurements on a feature or to extract quantitative information, features of interest require to be captured with sufficiently many pixels or voxels.

Considering a cone beam geometry with a non-magnifying detector, as used in all papers included in this thesis, high resolution is achieved through geometric magnification M, i.e. the object is placed close to the source with a larger distance to the detector. Thus, the effective pixel size $p_{\text{eff}} = P/M$ in the detector plane is the physical pixel size P divided by the magnification:

$$M = \frac{R_1 + R_2}{R_1}, \tag{2.3}$$

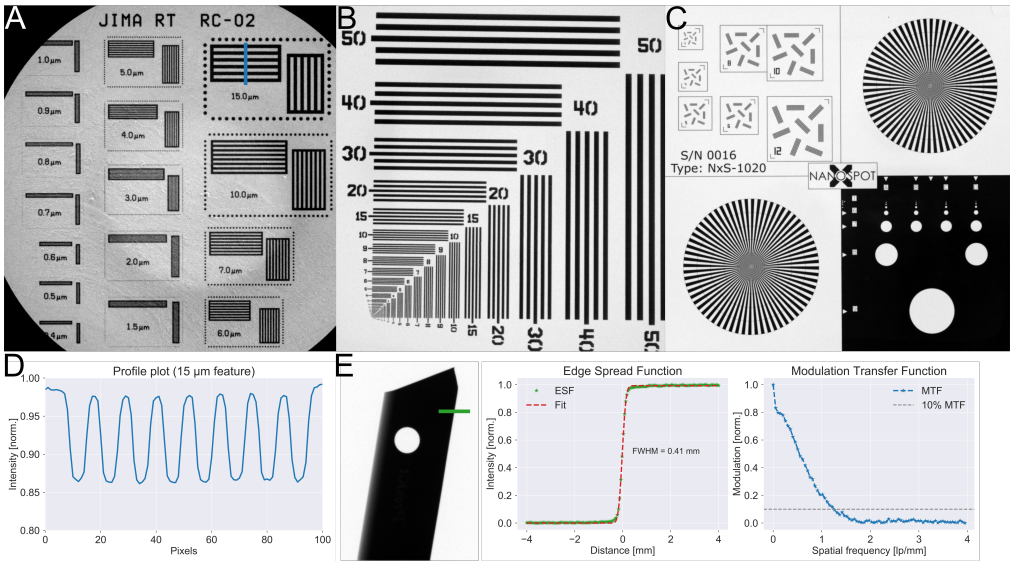

Figure 2.9: Different standard charts for resolution evaluation: **(A)** a JIMA RT RC-02 chart with features from 0.4 – 15 µm, **(B)** a test pattern from XRnanotech with lines and spaces from 0.2 – 50 µm, and **(C)** a nanoXspot gauge with 2 Siemens stars, line patterns from 3 – 12 µm, and differently sized holes for x-ray spot measurements. **(D)** Profile plot over the 15 µm feature of the JIMA chart (blue line). **(E)** Edge spread function and modulation transfer function measured on a slanted knife edge (green line) imaged with a FlatPanel detector at p_{eff} = 84.3 µm.

where R_1 is the source-object distance and R_2 is the object-detector distance, as indicated in Figure 2.7. Another effect that has to be considered is penumbral blurring, i.e. the projected x-ray spot on the detector may be larger than a single pixel, which contributes to blurring and thus limits the achievable resolution. In PB-PCI, described in Chapter 2.5.1, the effective propagation distance $z_{\text{eff}} = R_2/M$ scales with the magnification, thus the distances R_1 and R_2 can be optimised to maximise z_{eff} for a desired p_{eff}.

In 2D imaging, resolution can be expressed as the minimum detectable distance between two high contrast features as shown in Figure 2.9D. For this purpose, calibration phantoms are used, which typically consist of line patterns made from highly absorbing Tungsten or Gold on a Silicon membrane, as shown in Figure 2.9A-C. The result is often expressed in resolvable line pairs per millimetres (lp/mm). Commonly, the Modulation Transfer Function (MTF) is determined, which describes the response of the imaging system dependent on feature size. A convenient approach is the slanted edge method [Estribeau and Magnan (2004)], defined in ISO 12233, utilising slightly tilted sharp edges to calculate an Edge-Spread Function (ESF), describing the resolution, while also extracting a MTF curve, as shown in Figure 2.9E.

In 3D, the resolution is affected by the data processing and reconstruction plus effects occuring during the measurement, such as vibrations or drifts of the sample and stages, and defocusing or drift of the x-ray spot. While there are phantoms available, it is still difficult to consistently define the resolution of an imaging system in CT. An approach to

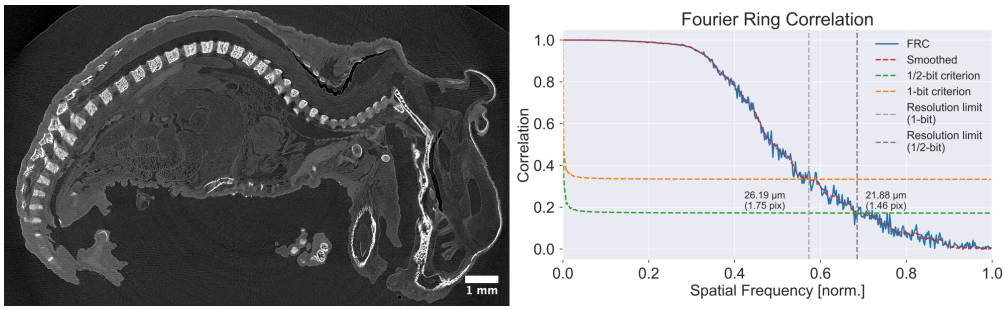

Figure 2.10: Resolution measured using Fourier ring correlation on a micro-CT scan of a paraffin embedded mouse fetus with a 20 µm x-ray spot and p_{eff} = 15 µm. The dataset has been split and two identical reconstructions have been performed from which two identical slices are correlated. To obtain the resolution limit of the slice, the last intersection of the FRC curve with a threshold criterion is used.

measure the resolution limit of a reconstructed dataset is Fourier Ring Correlation (FRC), which calculates the resolution of a slice as demonstrated in Figure 2.10, or Fourier Shell Correlation (FSC), which calculates the resolution in a volume [van Heel (1987)]. This method correlates two identical slices, or volumes, in Fourier space and compares the result to a threshold criterion yielding the smallest resolvable spatial frequency [van Heel and Schatz (2005)]. This approach was used in Papers III and VI.

Contrast describes how well a feature can be distinguished from the background or its surroundings. A common mathematical definition is the Weber contrast [Peli (1990)]:

$$C = \frac{I - I_{\text{bg}}}{I_{\text{bg}}}, \tag{2.4}$$

where the signal intensity I of the evaluated feature is compared to the signal intensity of the background I_{bg}. Another definition that is useful when dealing with periodic structures is the Michelson contrast [Michelson (1927)], often referred to as *visibility*:

$$V = \frac{I_{\text{max}} - I_{\text{min}}}{I_{\text{max}} + I_{\text{min}}}, \tag{2.5}$$

where the minimum I_{min} and maximum I_{max} intensities of a structure are compared.

Noise is manifested as an unwanted random signal obfuscating features and thus reducing the visibility in acquired images. It originates from photon noise, the measurement setup, e.g. thermal and readout noise of the detector, and image processing, e.g. upscaling or sharpening. Photon noise is caused by inherent randomness of the x-rays photons and can be approximated as Poisson or Gaussian noise [Lalush and Wernick (2004)]. To reduce image noise, assuming the geometry remains unchanged, the exposure time needs to be increased. A common approach to quantify noise is the Signal-to-Noise Ratio (SNR), which has a variety of definitions, but we used:

$$\text{SNR} = 20 \times \log \frac{s}{n_{\text{RMS}}}, \tag{2.6}$$

where s is the mean value of a region containing the object and n_{RMS} is the root mean square of the background, which yields a result expressed in dB. To quantify the contrast, the Contrast-to-Noise Ratio (CNR) [Ishitani and Sato (2007)] can be used:

$$\mathrm{CNR} = \frac{|s - n|}{\sigma_n}, \tag{2.7}$$

where n is the mean value of the background and σ_n is the standard deviation of the background.

A variety of techniques to reduce noise in acquired images and scans exists. Denoising typically has side effects like reduced image resolution. Common approaches are binning and median filtering, where neighbouring pixels are combined resulting in lower noise at the expense of resolution, or low-, high-, and band-pass filtering removing low or high frequency noise. More advanced filters are e.g.: total variation, bilateral filtering, wavelet denoising, and non-local means. The recently developed *noise2inverse* method [Hendriksen et al. (2020)], a self-supervised machine learning approach, has shown excellent performance for the denoising of tomography data.

2.5.3 Super-resolution

Super-resolution describes mathematical techniques to combine multiple slightly shifted low-resolution images into a high-resolution image [Milanfar (2010); Yoneyama et al. (2015)]. There are also a variety of machine learning-based algorithms that can produce a higher resolution image from a single low-resolution image [Dong et al. (2016)]. In the context of x-ray imaging, super-resolution effectively increases the Field-of-View (FOV) at a certain resolution, as long as the x-ray spot size is not the limiting factor. In the simplest case, the method works by acquiring a number of images with a sub-pixel shift, registering the shifts, perform upscaling on shifted high-resolution pixel grids, and combining the images [Park et al. (2003); Gilman et al. (2008)]. The PSF of an imaging system can be taken into account by several, mostly iterative, super-resolution algorithms, such as iterative back-projection [Irani and Peleg (1991)] or regularisation-based approaches [Sroubek et al. (2007, 2017); Sroubek and Milanfar (2012)]. The method is described in detail in Chapter 4.1 and was used in Papers I – III.

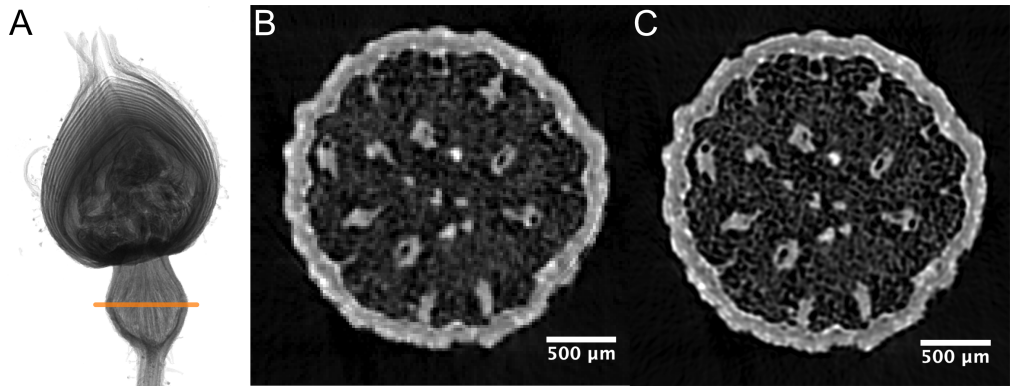

Figure 2.11: Example of super-resolution CT. **(A)** Radiography of a dried flower bud. **(B)** Reconstructed slice (orange line) from a regular CT scan with p_{eff} = 20 µm. **(C)** Reconstructed slice (orange line) from a super-resolution CT scan consisting of 4×4 images per scan with a resulting p_{eff} = 5 µm.

2.5.4 Energy-resolved imaging

Using a photon counting detector with multiple energy-discriminating thresholds, energy information can be obtained. Acquired images are split into energy bins by subtracting images with different thresholds from each other. The resulting images contain only photons in a certain energy range, which we refer to as *energy windows*. By exploiting absorption edges of different elements, characterised by abrupt changes in attenuation, just above the binding energy of the shells of an atom [Podgoršak (2009)], as shown in Figure 2.12A, these elements can be identified, which allows to decompose images and CT scans into concentration maps of different elements. By acquiring images with energies just below and above an absorption edge, as shown in Figure 2.12B, the element's difference in attenuation can be exploited to identify the specific element. This approach is best suited for CT, where each voxel in the reconstruction has its specific attenuation coefficient μ. When performing a decomposition, each voxels attenuation coefficient is expressed as the sum of the attenuation coefficients $\mu_{E,i}$ of a set of elements and their fraction f_i for a given number of elements i: $\mu_E = \sum \mu_{E,i} \times f_i$ [Alvarez and Macovski (1976); Badea et al. (2012)]. Paper III describes the approach in more detail and follows the method described by Badea et al. (2012). A variant of this approach is being used in clinical CT, typically referred to as dual-energy CT [Granton et al. (2008)], where either two different x-ray sources are used or the voltage of the x-ray source is changed for the second acquisition. However, by using detectors with sufficiently many energy thresholds, all the information can be extracted in a single scan using a single x-ray source.

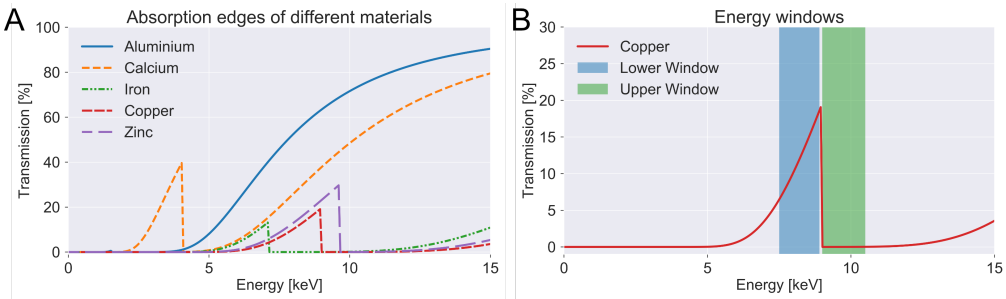

Figure 2.12: **(A)** x-ray transmission through 50 µm of different elements showing absorption edges at characteristic energies. **(B)** Placement of energy windows, i.e. upper and lower thresholds, around the absorption edge of Copper. Simulated data from Henke et al. (1993)

Alternatively, detectors like the Timepix [Llopart et al. (2007)] can acquire spectral information directly. Every pixel works, in principle, like a spectrometer. Compared to regular photon counting detectors, the these detectors not only count photons, but also the time the pulse generated by the photon stays above a threshold, which can then be related to an energy. This concept is referred to as Time-over-Threshold (ToT) and was developed for applications like particle tracking [Jakubek et al. (2008)], but has also found use in imaging [Navarrete et al. (2019); An et al. (2020); Dudak and Zemlicka (2022)].

2.6 Computed tomography

Computed Tomography (CT) is a method that reconstructs the internal 3-dimensional structure of an object imaged from different angles. The method was developed in the early 1970s by Hounsfield (1973), based on the mathematical foundation formulated by Radon (1986) in the 1910s. Image reconstruction is based on the Fourier slice theorem, which describes that the Fourier transform of a projection $P_\theta(t)$ through an object at an angle θ yields the values of a line at angle θ in Fourier space. Thus, by acquiring projections at different θ, the object is sampled in Fourier space and can, in principle, be reconstructed by an inverse Fourier transform [Kak and Slaney (2001)]. In practice, algorithms like Filtered Back-Projection (FBP) are used, since lower frequencies are sampled much more densely by this approach and thus need to be suppressed by a filter to obtain an adequate reconstruction [Tsui and Frey (2006)]. CT is a common diagnostic method in medicine, but also widely used in biomedical and material research and for industrial inspection [Christoph and Neumann (2018)].

2.6.1 Geometry and reconstruction

To perform a CT reconstruction, the measurement geometry has to be known precisely. The exact definitions of the geometry are often dependent on the used software toolkit. Here we follow the definitions from the ASTRA toolbox developed by van Aarle et al. (2015,

2016) as shown in Figure 2.13: the object is assumed to be stationary at origin, while source and detector rotate around the object with their motions described by vectors **S** and **D** in *x, y, z* directions. To model tilts of the rotation axis along and perpendicular to the beam direction, the detector plane is further described by the **U** and **V** vectors in *x, y, z* direction, describing the position from the centre pixel to a neighbour pixel in vertical and horizontal directions. It should be noted that the definitions used in the ASTRA toolbox use *y* as axis for the x-ray beam, while in x-ray systems, the *z* axis is commonly used as beam axis. With this approach all kinds of acquisition geometries, e.g. standard circular CT, helical CT, offset CT, etc., and imperfections, e.g. tilts of the rotation axis or misalignment of the detector, can be modelled and included in the CT reconstruction as shown by Samber et al. (2021).

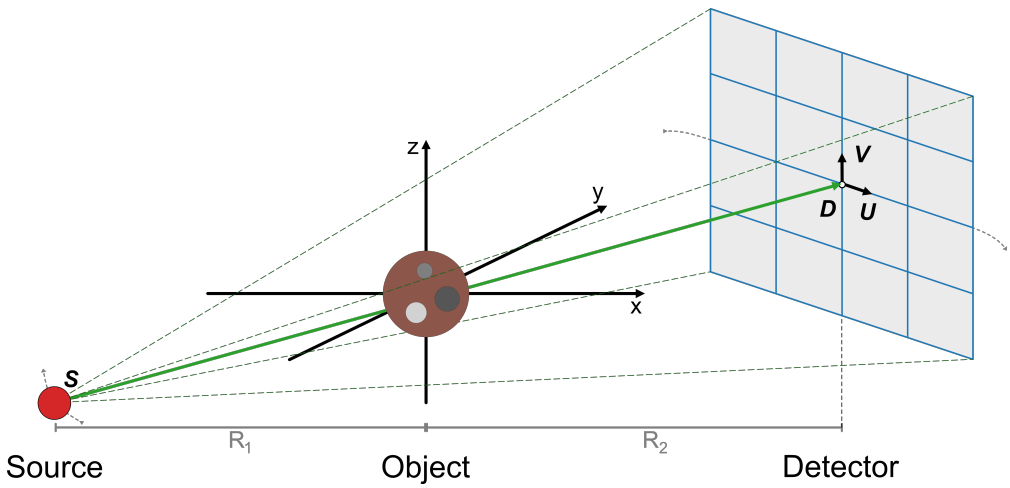

Figure 2.13: Sketch of the CT geometry used by the ASTRA toolbox. The object is assumed to be stationary while the source and detector rotate around it. Motion of source and detector is described using vectors for their positions $\mathbf{S_{x,y,z}}$ and $\mathbf{D_{x,y,z}}$ respectively. To account for tilts of the rotation axis perpendicular to beam direction, the $\mathbf{U_{x,y,z}}$ vectors are used describing the position of the centre detector pixel to its neighbour in xy plane. Tilt along the beam axis is represented by the $\mathbf{V_{x,y,z}}$ vectors describing the distances of the centre detector pixel to the pixel above.

To reconstruct CT scans acquired in cone beam geometry, commonly the Feldkamp-Davis-Kress (FDK) algorithm [Feldkamp et al. (1984)] is used. FDK provides an efficient implementation of FBP alongside assumptions to account for the diverging cone beam. Angular sampling of the object needs to be sufficiently dense to avoid artefacts in the reconstruction. The required angular sampling, equally spaced over 360 degrees, is estimated by $\frac{\pi}{2} s_{\text{pix}}$, where s_{pix} is the width of the object in pixels on the detector. It should be noted that FDK is only defined for circular trajectories of source and detector movement, i.e. in a laboratory scan, the object only rotates. Thus, reconstructions of more complex acquisition geometries will not be accurate and may exhibit artefacts or distortions.

2.6.2 Mechanical stability

Quality and resolution of a CT scan are affected by several factors in addition to the 2D performance of the imaging system, described in Chapter 2.5.2. A major aspect to consider, particularly for very high-resolution CT, is the thermal and vibration stability of the system. Thermal drift manifests itself as slow drifts through expansion or contraction of the equipment as a result of slight changes in temperature. However, these slow drifts can be corrected fairly easily, e.g. by acquiring alignment images at selected angles before or after the scan, comparing them to the projections, and then applying the measured shifts to the projections. Vibrations are much more difficult to correct. They can be caused by air flow, fans and pumps in equipment nearby, but also things like traffic on a nearby road. Assuming the image acquisition is sufficiently fast to sample vibrations, there are a few approaches to correct them, such as joint re-projection [Gürsoy et al. (2017)], distributed optimisation [Nikitin et al. (2021)], or phase symmetry [Pande et al. (2022)]. Generally, drifts and vibrations should be avoided in the design of the imaging system as much as possible. Setup stability and drifts are further discussed in Chapter 3.2. The x-ray source may also have an influence on the stability and resolution. Particularly nano-focus sources may experience a positional drift of the x-ray spot and de-focusing over time.

The parameters discussed above have a much more significant impact on very high-resolution CT system, such as a nano-CT targeting resolutions ≤ 1 µm. A micro-CT system with resolutions down to a few µm will be much less susceptible to drifts and vibrations. However, in both kinds of imaging systems, correct alignment of the CT geometry, i.e. position and tilts of the rotation axis and detector position, has a significant impact on the quality of the reconstruction. Ideally, the rotation axis and detector are aligned in the setup as precisely as possible. Calibration phantoms, typically consisting of a pattern of metal spheres, are a common way to extract tilts and positional offsets from a few projections as described by Yang et al. (2006); Bircher et al. (2019); Graetz (2021). With increasing resolution, this becomes increasingly difficult and may require correction in the reconstruction geometry.

2.6.3 Data processing and analysis

Pre-processing, i.e. processing of projections before reconstruction, includes a large number of possible steps. A typical pre-processing step is flat-field correction of the acquired raw images, i.e. division of the raw images with a flat-field image. When using scintillator-based detectors, the dark-field image, containing thermal and readout noise, is subtracted from the raw images and flat-field images first. Further steps include e.g. cropping, outlier removal, ring filtering, and phase-retrieval, and drift correction. Outliers are pixels that are over- or under-responsive, which have to be identified and then replaced with an average of their surrounding pixels. Pixels that are brighter or darker in most or all projections and could not be removed as an outlier will manifest as rings in the reconstructed slices,

or as stripes in the sinograms. Ring filters operate by finding and removing stripes from the sinograms using a variety of methods [Vo et al. (2018, 2021); Münch et al. (2009)]. If necessary phase-retrieval can be applied, as described in Chapter 2.5.1. Following, drift correction can be applied using. To find the centre-of-rotation, two projections 180 degrees apart can be compared and shifted to minimise the difference between them. However, this approach does often not work reliably for cone beam CT or low contrast objects. Thus, it is preferable to perform reconstructions of a set of single slices with varying shifts and evaluating the images visually or scoring the images based on sharpness. There are a variety of tool kits providing pre-processing algorithms and interfaces to reconstruction toolboxes [Micieli et al. (2019); Hendriksen et al. (2021); Jørgensen et al. (2021); Vo et al. (2021)].

Post-processing and analysis of reconstructed volumes is highly dependent on the data quality and desired analysis. Processing can range from image filtering and denoising to binarisation and morphological operations. There are algorithms and toolboxes to extract certain features from volumes, e.g. many image processing and analysis methods are implemented in the *scikit* library for Python [Gouillart et al. (2016)], or in more specialised toolboxes such as the PoreSpy package for analysis of porous materials [Gostick et al. (2019)]. The Fiji software developed by Schindelin et al. (2012) also provides a large variety of plugins for image analysis. Commercial tools are also available, such as Dragonfly (Object Research Systems Inc., Canada), Avizo/Amira (Thermo Fisher Scientific Inc., USA), and VG Studio (Volume Graphics GmbH, Germany).

3 Design and verification of laboratory x-ray CT systems

3.1 Micro-CT

The developed micro-CT system is built for biomedical imaging with resolutions down to 5 µm and main energies of 10 – 30 keV, with the source at 70 kV. All experiments included in thesis have utilised photon counting detectors. This setup has been used in Papers I – V.

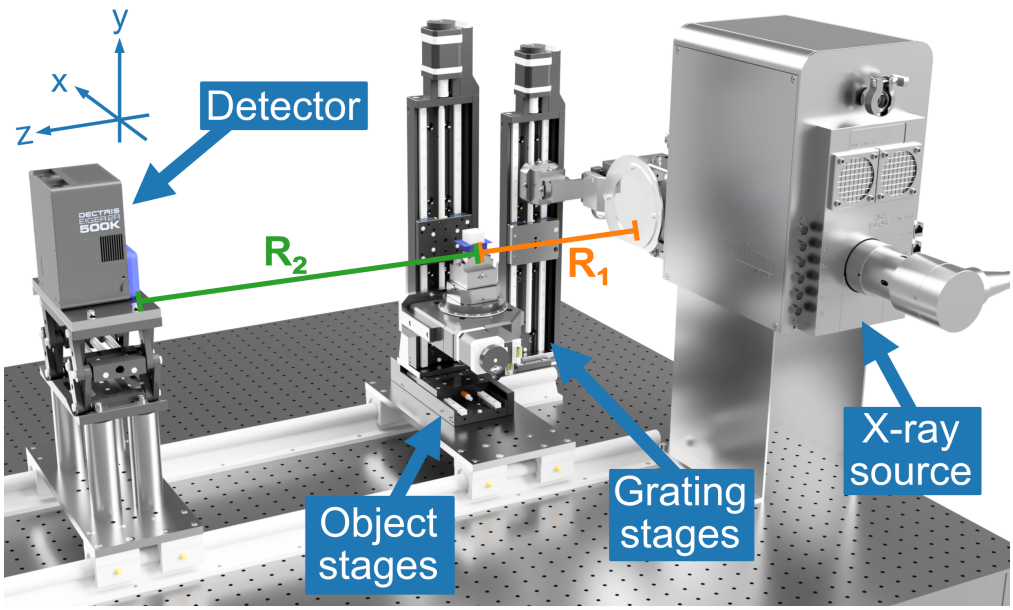

Figure 3.1: Render of the micro-CT system consisting of the x-ray source, detector, object holder, and grating holder.

3.1.1 Equipment

The setup is based on a prototype source from Excillum AB on the basis of a MetalJet D2 [Hemberg et al. (2003)], but with a conventional solid metal target. The target has been designed during this thesis work and utilises a thin Tungsten layer on a diamond carrier brazed to a larger copper rod attached to water cooling, for higher power loading capability. The x-ray source also allows electromagnetic stepping of the electron beam on the target, which gives a movable x-ray spot.

A variety of photon counting detectors have been used, initially a Pilatus 100K (Dectris Ltd.) [Henrich et al. (2009)], which was then replaced with an Eiger 2R 500K (Dectris Ltd.) [Johnson et al. (2014)]. Both detectors utilise a Silicon sensor making them very efficient for lower x-ray energies. For a brief period, a Lambda 350K (X-Spectrum GmbH) photon counting detector with a Gallium Arsenide sensor [Pennicard et al. (2012)] was used, provided as a loan.

A rail system, as shown in Figure 3.1, is used to manually translate the detector and object stages along the optical axis of the x-ray source. The object is mounted on a goniometer head (Huber Diffraktionstechnik GmbH, Germany) placed on a rotation stage and linear stages (Owis GmbH, Germany). Additional linear stages have been used in Paper II to include a grating into the setup.

3.1.2 Distances and resolution

The primary detector used was the Eiger 2R 500K, which has 1028 $\times$ 512 pixels with a size of 75 µm resulting in an active area of 77.1 $\times$ 38.4 mm^2. For the full detector to be illuminated by x-rays, it needs to be placed 0.55 m from the source. The closest position an object could be placed at is 0.1 m resulting in a magnification of $M = 5.5$ and an effective pixel size of $p_{\text{eff}} = 13.6$ µm, which yields a FOV of 14 $\times$ 7 mm^2. The measurements presented in Papers III – V utilised longer source-object distances R_1, i.e. lower geometric magnification to fully cover larger objects. To increase the achievable resolution, the source-detector distance can be increased, which also increases absorption of x-rays in air and requires to increase the exposure time to achieve the same contrast and noise as at shorter distances. Thus, it is desirable to keep the system as compact as possible. Experiments with the Pilatus detector in Papers I and II were conducted with a source-detector distance of 1.53 m, since the grating period had to be aligned with the 172 µm detector pixels. While Paper I does not use a grating, the same distances have been chosen as in Paper II. This is further discussed in the corresponding papers and Chapters 4.1.2 – 4.1.3.

3.1.3 System performance

The resolution of the micro-CT system is evaluated using a nanoXspot gauge, shown in Figure 2.9C. The detector was moved to 0.73 m from the source and the gauge was placed as close as possible to the source at about 60 mm resulting in $p_{\text{eff}} \approx 6$ µm. The image of the Siemens star (Figure 3.2) shows that the 8 µm lines can be clearly resolved, while the 6 µm lines can almost be resolved. Evaluating the line patterns (Figure 3.2) and plotting line profiles through the 12, 10, and 8 µm features show that the three features can be resolved. The profile plot through the 8 µm feature indicates that the limiting factor may be p_{eff}. Assuming a Gaussian-shaped x-ray spot, about half the FWHM of the spot is the best achievable resolution, i.e. 5 µm when considering a 10 µm x-ray spot, which appears reasonable considering the resolved 6 µm, and partially resolved 4 µm, lines in the Siemens star.

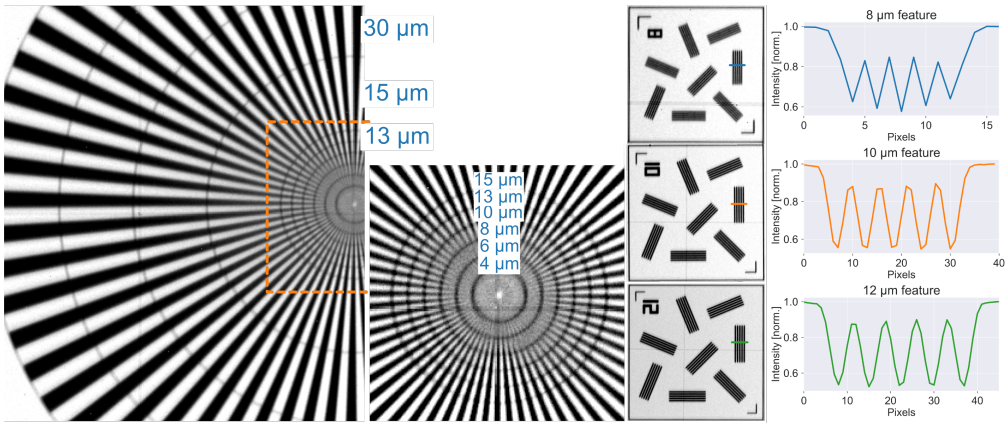

Figure 3.2: Achievable resolution of the micro-CT system measured using a Siemens star and line patterns on a nanoXspot gauge. The source was calibrated to a spot size of 10 µm at 70 kV. The Eiger detector was used and placed 0.73 m from the source, the gauge was placed about 60 mm from the source. In the Siemens star, the smallest visible pattern is 6 µm and in the line patterns, features down to about 8 µm can be clearly separated.

3.2 Nano-CT

A significant part of this thesis is the development of a nano-CT system targeting much higher resolution and smaller objects than the micro-CT, described in Chapter 3.1. Designing a high-resolution CT system comes with a variety of additional challenges regarding the stability and precision of the system. Paper VI describes the implementation of the system in detail.

3.2.1 Design considerations

This setup relies on high geometric magnification to achieve high resolution on a detector with comparably large pixels. Thus, being able to place objects within a few millimetres or less than a millimetre from the source is crucial to achieve reasonable source-detector distances as shown in Figure 3.3A. Figure 3.3B-C show the achievable p_{eff} for different source-object distances considering an Eiger detector and the scintillator-based GSense 16M (Photonic Science Ltd.). While the scintillator detector allows for a more compact system due to its smaller pixels, it should be noted that the efficiency of the Eiger detector is significantly higher and the noise is lower, as discussed in Chapter 2.4.

Stability of the system becomes a significant concern. The system is built in a low vibration environment placed on an optical table with air cushioned feet. Air flow is limited by a cabinet placed around the system. There is no active temperature control of the enclosure in the current system besides the ventilation of the room. Thermal expansion, mainly of aluminium used in most of the equipment, by a temperature change of a fraction of a degree can cause drifts on the micrometer scale, which can have a significant impact on the resolution of the system. Drifts are corrected using alignment images acquired with

10 degree spacing before and after the scan, which are cross-correlated with the projections resulting in corrections in x, y directions for the projections, as shown in Figure 3.4.

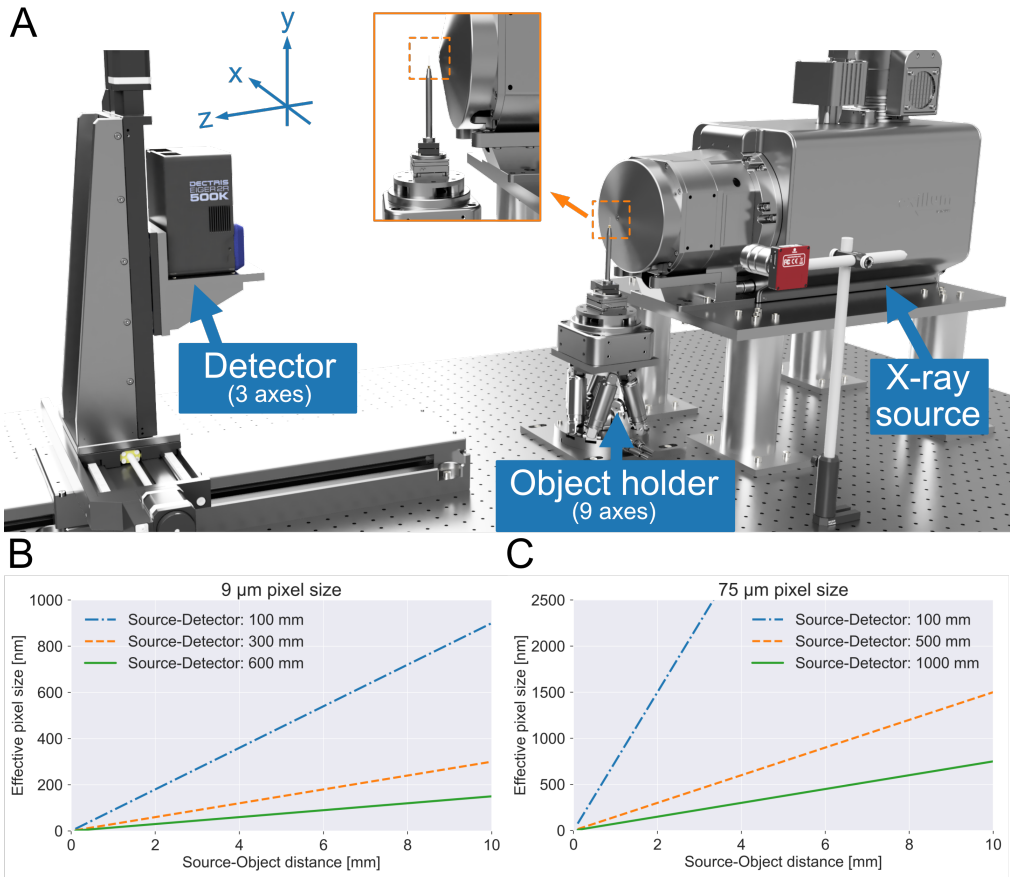

Figure 3.3: (A) Render of the nano-CT system consisting of the x-ray source, detector holder motorised in x,y,z directions, and object holder consisting of a hexapod with 6 axes, an air bearing rotation stage and a dual-axis piezo stage for fine alignment. The orange square shows a zoom in to the sample mount close to the source. Achievable effective pixel sizes for different source-object and source-detector distances using **(B)** a detector with 9 µm pixel size and **(C)** a detector with 75 µm pixel size.

3.2.2 Equipment

The nano-CT system is based on the NanoTube N2 60 kV (Excillum AB, Sweden), a transmission tube using a thin Tungsten layer on a diamond window allowing to place the object less than 1 mm from the source. The tube can achieve focal spots from 300 – 1200 nm resulting in a maximum achievable resolution of 150 nm (lines and spaces measured on a 2D resolution chart). The source produces a Tungsten emission spectrum with bremsstrahlung up to the selected acceleration voltage, similar to the spectrum shown in Figure 2.4. Hence, the main energy in the spectrum is around 10 keV.

Two detectors are considered: the photon counting Eiger 2R 500K, introduced in Chapter 3.1, and the GSense 16M (Photonic Science Ltd., UK) using a thin Gadox scintillator. The GSense detector has significantly smaller pixels at 9 µm and a large 4096 $\times$ 4096 pixel sensor. Both detectors have their maximum detection efficiency at around 10 keV. However, the Eiger detector has a significantly higher efficiency. Additionally, it produces less noise making it the preferred choice for very low density objects, e.g. paraffin embedded tissue biopsies, despite the longer source-detector distance required to achieve high resolution.

To mount objects as close to the source as possible, a variety of stages are used. The base is a H-811 hexapod (Physik Instrumente GmbH, Germany) providing translation in *x,y,z* direction as well as allowing to tilt the rotation axis perpendicular and along the beam, denoted as *u* and *v* axes respectively. On top of the hexapod, a RT100S air bearing rotation stage (LAB Motion Systems, Belgium) is placed, denoted as *ry* axis. Air bearing stages allow for higher positional stability, position repeatability, and precision. Fine alignment of the object is realised using a PILine U-723 high precision dual-axis piezo stage (Physik Instrumente GmbH, Germany) placed on top of the rotation axis, providing two extra axes perpendicular and along beam direction, named *fx* and *fz* respectively. Using these extra axes, the object or a specific feature of the object can be centred on the detector.

The detector is motorised in *x,y,z* directions, referred to as *dx, dy, dz*, to allow fine tuning of p_{eff} by quickly changing the source-detector distance. Further, this also allows to quickly align the detector to the optical axis of the system. This is realised using three linear stages (Owis GmbH, Germany), where the *dz* stage has a range of 0.6 m to allow for a large range of source-detector distances.

3.2.3 System performance

The temperature of the whole room is kept reasonably constant by a ventilation system at around 21.5 °C $\pm$ 0.12 °C measured over 160 h with sampling in a 5 s interval, as shown in Figure 3.4. Accessing the setup for longer times may cause temperature changes and require a longer time for the room to return to equilibrium. No significant temperature variations or fast changes could be observed, i.e. it is expected that any experienced thermal drift will be minor and gradual. Measuring the drift experienced by an object over 10 h during a CT scan (Figure 3.4) shows a few µm of drift in *x,y* directions. Drifts are measured by a cross-correlation of the projections with alignment images acquired before and after the scan in angular steps of 10°. The measured drifts include thermal drift as well as all other effects the system experiences, e.g. aberrations of the stages, drift of the x-ray spot, etc. However, the drift correction method using alignment images, detailed in Chapter 2.6 and Paper VI, appears to be sufficient to correct the drifts experienced by the system.

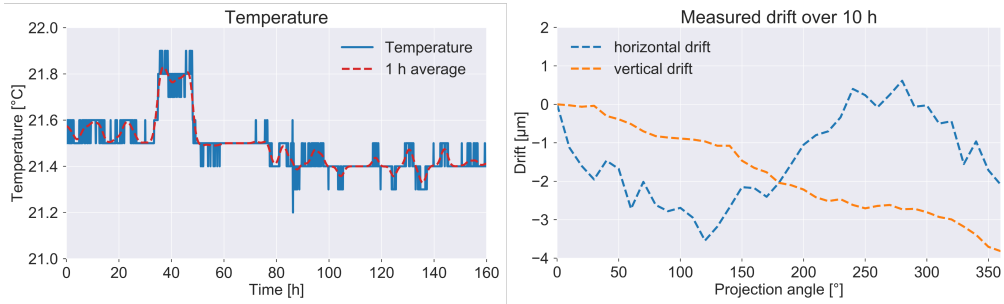

Figure 3.4: Environmental temperature in the experimental hutch over 160 h with a mean temperature of 21.5 °C and a standard deviation of ± 0.12 °C and measured drift of projection images during a 10 h CT scan using the Eiger detector with p_{eff} = 626 nm.

The achievable resolution in 2D imaging has been quantified using a JIMA RT RC-02 and a XRnanotech chart consisting of line patterns in different sizes. On the JIMA chart, the smallest line patterns (0.5 µm and 0.4 µm, shown in Figure 3.5A) could be easily resolved on both detectors as shown by the line plots in Figure 3.5B. It could also be observed that the Eiger detector achieves a higher visibility of approximately 8 % as compared to 3 % with the GSense detector, considering the 0.5 µm feature using Equation 2.5, while requiring a shorter exposure time despite the longer required distance from source. To image the XRnanotech chart (Figure 3.5C,E), the detectors were placed so that p_{eff} of approximately 50 nm or 150 nm was achieved for the GSense and Eiger detectors respectively, corresponding to the maximum achievable distance of the system at the moment. To achieve higher resolution, the detector z stage can be moved further away from the source. Both detectors managed to resolve the 200 nm features in both directions, as shown in Figure 3.5D for the GSense detector and in Figure 3.5F for the Eiger detector. Again, the Eiger detector (Figure 3.5E-F) achieves a higher visibility.

To measure the resolution in CT applications using actual biomedical samples, FRC is used, as discussed in Chapter 2.5.2, utilising a 0.5 mm biopsy punch from a paraffin embedded cow lung. The lung sample is taken from the project described in Paper V and is detailed in Chapter 4.3. Using the Eiger detector, a p_{eff} of 683 nm was achieved by placing the object 3.54 mm from the source and the detector at 388.1 mm from the source. The source was calibrated to a spot size of 600 nm at 60 kV acceleration voltage and 3200 projections with an exposure time of 20 s were acquired. Using the GSense detector, a p_{eff} of 321 nm was achieved with the object at 4.25 mm from the source and the detector at 238.15 mm from the source. The source was calibrated to a spot size of 400 nm at 60 kV acceleration voltage and 2800 projections were acquired with an exposure time of 16 s. The scan times could have been reduced by moving the object closer to the source, which was not possible due to the mounting of the object.

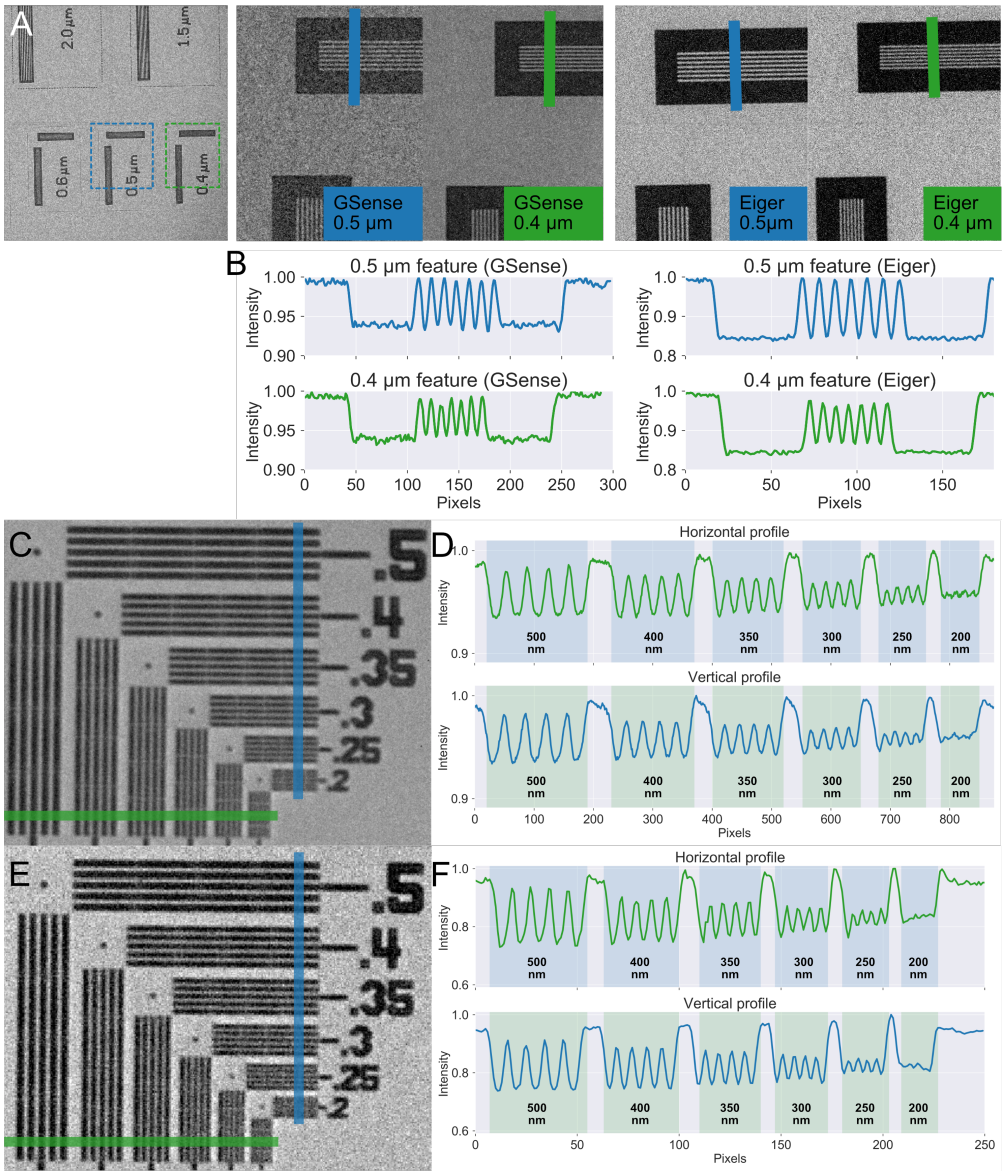

Figure 3.5: Achievable resolution of the nano-CT system evaluated with **(A)** JIMA RT RC-02 chart for both available detectors. **(B)** Line profiles from the 500 nm and 400 nm features for both detectors. **(C)** XRnanotech chart imaged with the GSense detector. **(D)** Horizontal and vertical line profiles from (C). **(E)** XRnanotech chart imaged with the Eiger detector. **(F)** Horizontal and vertical line profiles from (E).

Evaluating the resolution of scans with the Eiger detector using FRC on reconstructed slices, as shown in Figure 3.6A-B, demonstrated a resolution limit of 840 nm corresponding to $1.24 \times p_{\text{eff}}$ when using a reconstruction with absorption contrast (Figure 3.6C). By applying phase-retrieval, additional blur is expected, which can be

partly removed by unsharp masking, as discussed in Chapter 2.5.1. Hence, performing a reconstruction with phase-retrieval and unsharp masking yielded a resolution limit of 880 nm (Figure 3.6C) corresponding to 1.29 $\times$ p_{eff}, i.e. almost the same as without phase retrieval, while providing significantly better contrast (Figure 3.6B). Performing the same evaluation using the scan acquired with the GSense detector shows that the resolution limit is 870 nm (Figure 3.6F) corresponding to 2.71 $\times$ p_{eff}, which matches the expected PSF of the detector of approximately 3 $\times p_{\text{eff}}$.

It can also be observed that performing phase-retrieval introduces a cupping artefact, i.e. the centre of the object appears darker as seen in Figure 3.6E. Phase-retrieval was set to achieve a comparable contrast increase in both scans. However, the difference may be caused by the different energy response of the detectors. Calculating the SNR and CNR using Equations 2.6 and 2.7 respectively yields a comparable SNR for detectors of approximately 49 dB, which is unexpected since the scan with the Eiger detector (Figure 3.6A-B) looks significantly less noisy than the scan with the GSense detector (Figure 3.6D-E). However, the scans from the Eiger detector have a higher CNR of 3.65 (dye filled vessels) or 1.73 (tissue) than the scans with the GSense detector with 0.62 (dye filled vessels) or 0.72 (tissue). Further, performing phase retrieval increased the CNR of the Eiger scans by a factor of about 3.5 compared to a factor 2 increase for the GSense detector. SNR and CNR of the different detectors is discussed in more detail in Paper VI.

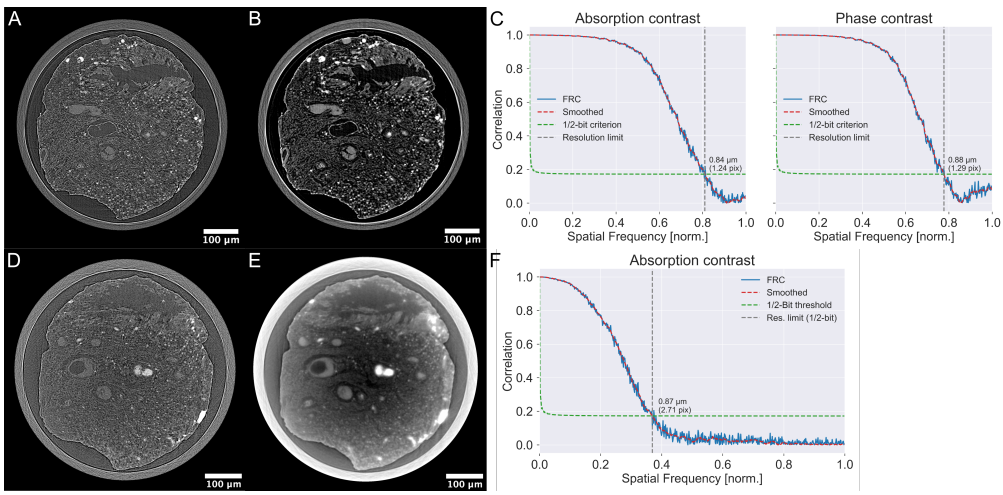

Figure 3.6: Achievable resolution of the nano-CT evaluated with Fourier Ring Correlation using a 0.5 mm biopsy punch from a cow lung. **(A)** Reconstructed slice using absorption contrast, scanned with the Eiger detector at 0.683 µm voxel size. **(B)** Reconstructed slice with phase contrast. **(C)** Fourier Ring Correlation of the Eiger scans with absorption contrast and phase contrast. **(D)** Reconstructed slice using absorption contrast, scanned with the GSense detector at 0.321 µm voxel size. **(E)** Reconstructed slice with phase contrast. **(F)** Fourier Ring Correlation of the absorption contrast scan.

4 Imaging applications

4.1 Super-resolution x-ray imaging

4.1.1 The super-resolution method

There are a variety of methods to achieve super-resolution, as already described in Chapter 2.5.3. While most approaches incorporate corrections for the detector PSF, estimation of a super-resolution image can be simplified when using a photon counting detector with a box-like PSF as discussed in Chapter 2.4. Thus, the estimation of super-resolution images, as used in Papers I – III, has been simplified to:

(i) precise registration of shifts between images

(ii) interpolation on shifted high-resolution grids

(iii) estimation of a super-resolution image by averaging of high-resolution images

Image registration has been performed with cross-correlation as described by Guizar-Sicairos et al. (2008). The precision of the used method can potentially have a significant impact on the quality of the result, thus the result of this step needs to be carefully evaluated. For the interpolation step, mainly spline interpolation has been used. However, a variety of available standard interpolation methods have been evaluated in Paper I. The theoretical number of shifted images n_{img} required to achieve a certain increase in resolution R has been described by Sroubek and Flusser (2005) to be $R = \sqrt{n_{\text{img}}}$, i.e. to increase the resolution by a factor of 4, at least 16 shifted images are required.

Papers I – III have shown that this approach works well in the micro-CT setup, described in Chapter 3.1, where the x-ray spot is small, the detector pixels are large, and the magnification is limited. In this case, a single pixel PSF can be assumed. However, Paper III has shown that, at higher magnifications, penumbral blurring has to be considered.

4.1.2 Optimisation of acquisition parameters

While super-resolution is well understood and characterised in conventional imaging and photography, it is still a somewhat uncommon technique in x-ray imaging. While the basic concepts are identical, introducing a photon counting detector is a significant difference. Thus, an experimental evaluation of different acquisition and processing parameters was performed in Paper I to better understand their influence on the estimated super-resolution image, to find parameters for future experiments, and to find metrics to evaluate the resulting images.

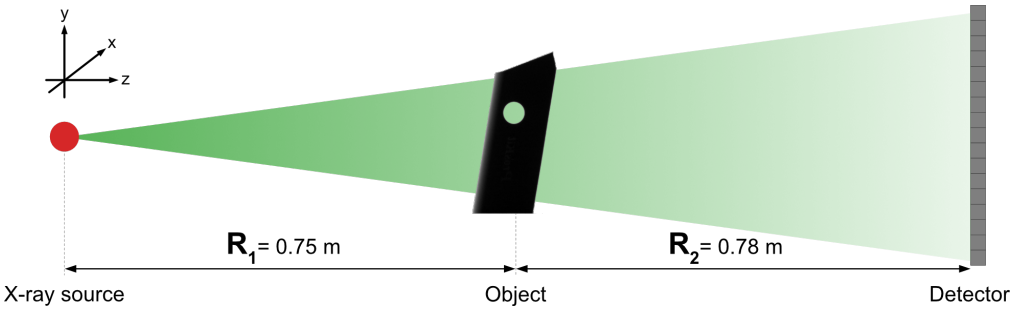

Figure 4.1: Sketch of the setup used for super-resolution experiments with a Pilatus detector placed 1.53 m from the source to match the geometry used in Paper II. For MTF measurements, a knife edge (as shown above) was used. The remaining measurements utilised a dried rose bud.

Experiments were performed in the micro-CT setup described in Chapter 3.1 using a Pilatus 100K detector, with the geometry shown in Figure 4.1. The same geometry as in Paper II was used, which had the detector placed at 1.53 m from the source and the sample at 0.75 m from the source resulting in a magnification of 2.04 and thus p_{eff} = 84.3 µm. Parameters that were evaluated are:

(i) interpolation method

(ii) interpolation factor

(iii) number of low-resolution images

(iv) shift distance between low-resolution images

As default parameters, a regular 4×4 grid of images with a total shift of 3 pixels in *x, y* direction and 4× interpolation are used. Where a 4× resolution increase from 16 images is a compromise of measurement time and resolution gain. A total shift of 3 pixels has been used since it was found to work well in Paper II. Translation of the sample image on the detector is achieved through electromagnetic source stepping. The electron beam hitting the target inside the source is moved using the advanced electron optics of the source, as described in Chapter 2.3. Using this approach, no mechanical motion of the sample is required. A similar approach had been demonstrated by Harmon et al. (2015) by adding an external coil to an x-ray source.

To evaluate the effect of the different parameters on estimated super-resolution images, a MTF is calculated using the slanted edge method from a knife blade (as shown in Figure 4.1), SNR, CNR, and radial power spectra are calculated from images of dried flower buds. The evaluations have shown that the radial power spectra do not show any significant differences when varying the parameters, while SNR and CNR mostly show small variations. The experiments have shown that the MTF and CNR are the most meaningful measures to evaluate the experiments and are shown in Figure 4.2.

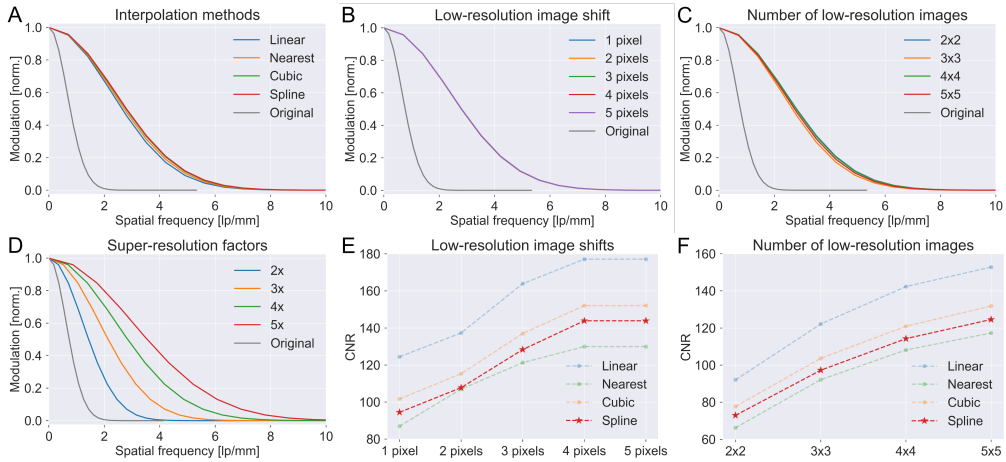

Figure 4.2: Main measurements of super-resolution parameters. **(A)** MTF measured using different interpolation methods with 4×4 images and 4× upscaling. **(B)** MTF measured using different shifts between 4×4 low resolution images for 4× upscaling using spline interpolation. **(C)** MTF measured using a varying amount of low-resolution images for 4× upscaling using spline interpolation. **(D)** MTF measured using different upscaling factors for 4×4 images and spline interpolation. **(E)** CNR measured corresponding to (B). **(F)** CNR measured corresponding to (C).

From the interpolation methods evaluated, spline has performed best visually and in terms of MTF and CNR, which has also been used in Paper II. The interpolation methods show only a very minor effect on the MTF (Figure 4.2A) with a minimally better performance of spline interpolation. Evaluating the shifts between the low-resolution images (Figure 4.2B), the MTF shows no significant difference, while the CNR (Figure 4.2E) shows a contrast improvement with increasing shifts. However, when evaluating the resolution in Paper III, a 1 pixel total shift has been shown to be preferable. Varying the amount of low-resolution images (Figure 4.2C), the MTF shows a very similar performance, almost independent of the number of images. When also considering the CNR (Figure 4.2F), it can be seen that the contrast improves with increasing number of low-resolution images. This may, however, only be an effect from the increased total exposure time when increasing the number of images. When varying the interpolation factor (Figure 4.2D), using 4×4 images, the MTF improves with increasing interpolation. This indicates that the resolution limit in the given geometry is defined by the size of the x-ray spot and not the pixel size. Thus, in this case, the potential maximum resolution increase of $\sqrt{n_{\text{img}}}$, as discussed above, does not appear to necessarily be the limit.

Considering the geometry, with a magnification of 2.04 and a p_{eff} of 84.3 µm, and the small x-ray spot size (10 µm), the limitations regarding the resolution are mainly due to the pixel size of the detector. While penumbral blurring is insignificant at the used geometry and the detector PSF can be assumed to be close to a single pixel, a resolution increase of down to, in principal, 5 µm should be achievable, which would correspond to a 17× increase. The practicality of which is questionable, since the number of extra images required would be significant.

4.1.3 Super-resolution in single-grating imaging

To gain access to the dark-field and differential phase contrast signals, gratings are used as described in Chapter 2.5.1 and discussed in detail in Paper II. Most grating approaches require precise alignment of, typically, multiple gratings and multiple acquisitions at different grating positions to sample the full FOV due to parts of the detector being covered by the gratings. The single-shot approach developed by Wen et al. (2008, 2010) simplifies the setup by using a single absorption grating with a period, which is resolved on the detector and aligned to the detector pixels. Thus, the three modalities: absorption, dark-field, and differential phase can be obtained by extracting spatial harmonics from the Fourier transform of a single acquisition. Further, this approach works with larger grating periods, which are much simpler to manufacture. The disadvantage of this approach is the reduction in resolution defined by the number of pixels on the detector the grating period is aligned to and lower sensitivity. Particularly the phase contrast was quite poor with the available 36 µm period grating.

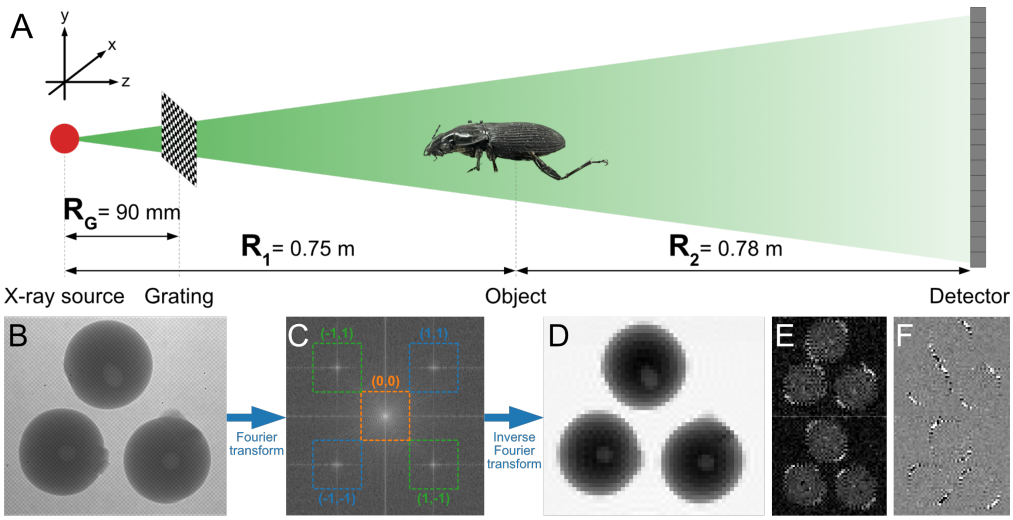

Figure 4.3: Grating setup and concept of the single-shot method. **(A)** Sketch of the used setup with a 2D checkerboard grating with 36 µm period placed 90 mm from the source aligned to a Pilatus detector placed 1.53 m from the source. **(B)** 2D projection of 3 plastic spheres with the grating pattern visible. **(C)** Fourier transform of (B) showing 0^{th} and 1^{st} order spatial harmonics. **(D)** Absorption image extracted from the 0^{th} order harmonic (orange). **(E)** Dark-field images extracted from the 1^{st} order harmonics (blue and green). **(F)** Differential phase extracted from the 1^{st} order harmonics (blue and green).

By using the Pilatus photon counting detector and a 2D absorption grating with a checkerboard pattern, the grating period could be aligned to 4×4 pixels on the detector while still being resolvable. Hence, extracting the image modalities reduces the resolution by a factor of 4, which was then compensated through using super-resolution. The used grating had a period of 36 µm and could be placed about 90 mm from the x-ray source. Given the 172 µm pixel size of the detector, a distance of 1.44 m between the grating and the

detector was necessary to magnify the 36 µm grating period onto 4×4 pixels on the detector. Instead of a single image, 4×4 shifted images were acquired, the three modalities were extracted for each position, and a super-resolution image was estimated for each modality as described in Chapter 4.1.2.

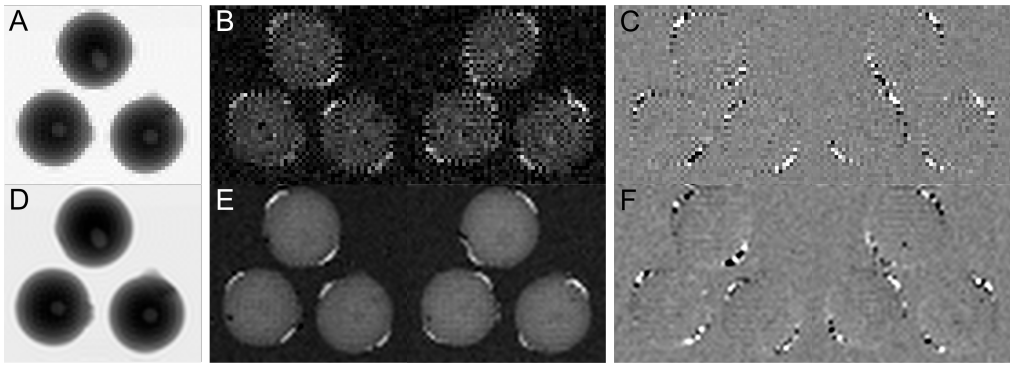

Figure 4.4: Demonstration of super-resolution using the single-shot method applied to a test sample consisting of three plastic spheres. Three modalities extracted from a single image: **(A)** Absorption, **(B)** Dark-field in two perpendicular directions, and **(C)** Differential phase in two perpendicular directions. Applying super-resolution using 4×4 acquisitions: **(D)** Absorption, **(E)** Dark-field, and **(F)** Differential phase. *Images adapted from Paper* II.

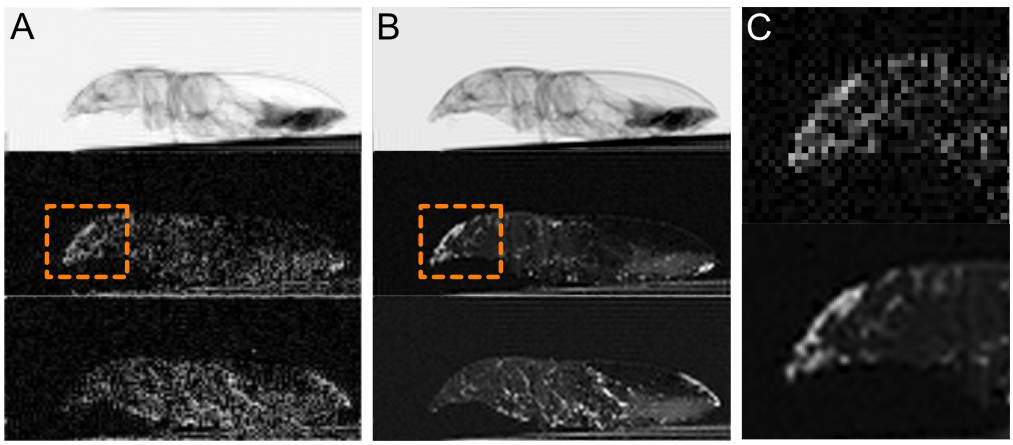

Figure 4.5: Super-resolution dark-field imaging of a beetle. **(A)** Absorption and dark-fields from a single image. **(B)** Super-resolution absorption and dark-fields from 4×4 images. **(C)** Zoom in on the head of the beetle, marked in orange in (A) and (B), of a single image and super-resolution dark-field. *Images adapted from Paper* II.

The method was applied to a test sample, consisting of plastic spheres shown in Figure 4.4, and a beetle as a biomedical sample shown in Figure 4.5. Comparing the extracted absorption and dark-field images from a single exposure with 4× spline interpolation and 4× super-resolution shows that the resolution and contrast are significantly improved when using super-resolution. Only applying interpolation to a single acquisition using the same total exposure time as for 16 shifted acquisitions, it could be observed that super-resolution

performs significantly better. The differential phase contrast was observed to be very poor in all cases, which is due to the large grating period and distance between the object and the grating. When acquiring multiple images, the required grating alignment can be further relaxed by using UMPA [Zdora et al. (2017)] to extract the image modalities.

4.1.4 Super-resolution x-ray tomography

To evaluate super-resolution in tomography, two approaches are compared: (i) creating super-resolution projections before performing a reconstruction and (ii) reconstruction onto a finer grid with the ASTRA toolbox. The advantage of handling the resolution increase via ASTRA is that only a single projection per angle is required instead of acquiring a grid of shifted images for every projection. Further, two geometries are compared as shown in Figure 4.6, where the source-detector distance is kept at 0.55 m: (i) a lower magnification geometry that limits the limits the projected spot size on the detector to about $1/2$ pixels with R_1 = 0.346 m and M = 1.59 and (ii) a higher magnification geometry with the source-object distance R_1 = 0.15 m and thus a magnification of $M = 3.67$. Contrary to the previous experiments described in Chapters 4.1.2 – 4.1.3 and covered in Papers I and II, the Eiger 2R 500K detector was used, which has 75 µm pixels and a sensor size of 1028 $\times$ 512. The detector is described in more detail in Chapter 3.1. Additional measurements were performed with a Lambda 350K detector, which has 55 µm pixels and is also described in more detail in Chapter 3.1.

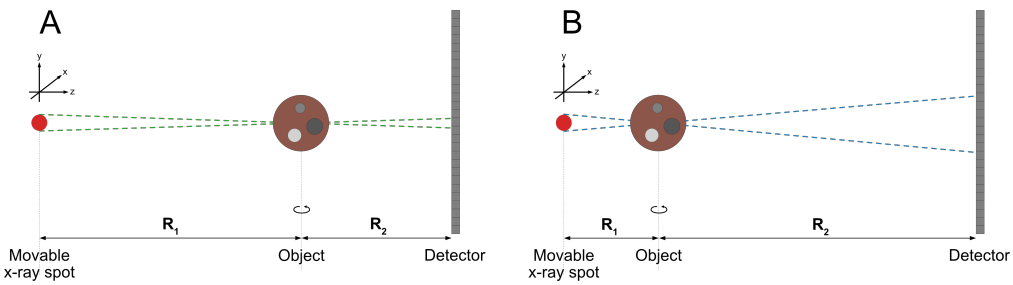

Figure 4.6: Sketch of the two different geometries used for super-resolution CT. **(A)** Low-magnification geometry with lower resolution, but limited penumbral blurring. **(B)** High-magnification geometry with higher magnification, but more penumbral blurring.

Scans were performed using a 4×4 grid of images per projection with total shifts in the range of 1 – 3 pixels and 4× upscaling. At lower magnification, an additional scan was performed using a 6×6 grid and 6× upscaling. Regular and upscaled reconstructions were performed utilising the first image from the acquisition grid. The x-ray source was calibrated to a 10 µm spot at 70 kV. At high magnification, p_{eff} is 20.45 µm, which is then reduced using super-resolution to p_{super} = 5.11 µm. At low magnification, the p_{eff} of 47.18 µm is reduced to a p_{super} of 11.8 µm and 7.86 µm for 4× and 6× upscaling respectively. For the additional scans performed with the Lambda detector, R_1 was increased to 0.37 m

to limit penumbral blurring to the same 1/2 pixels as for the Eiger detector. This resulted in p_{eff} = 37.5 µm and p_{super} = 9.37 µm with 4× upscaling.

To estimate the resolution, two approaches were used: (i) first a more conventional approach calculating the ESF from a sharp edge in a reconstructed slice and (ii) the resolution limit of a slice was calculated using FRC. To extract the resolution from an ESF, a step function is fitted to a sharp edge and the characteristic width σ is extracted from which the Full Width at Half Maximum (FWHM) = 2.35σ is calculated. However, this approach relies on the quality of one specific feature in a specific location of a reconstructed slice. Hence, FRC is used to obtain the resolution limit considering the overall slice. For this approach, the projections were split and two identical reconstructions were performed. Then, two identical projections were aligned using an Affine transform, correlated using FRC, and compared to the 1-bit threshold criterion.

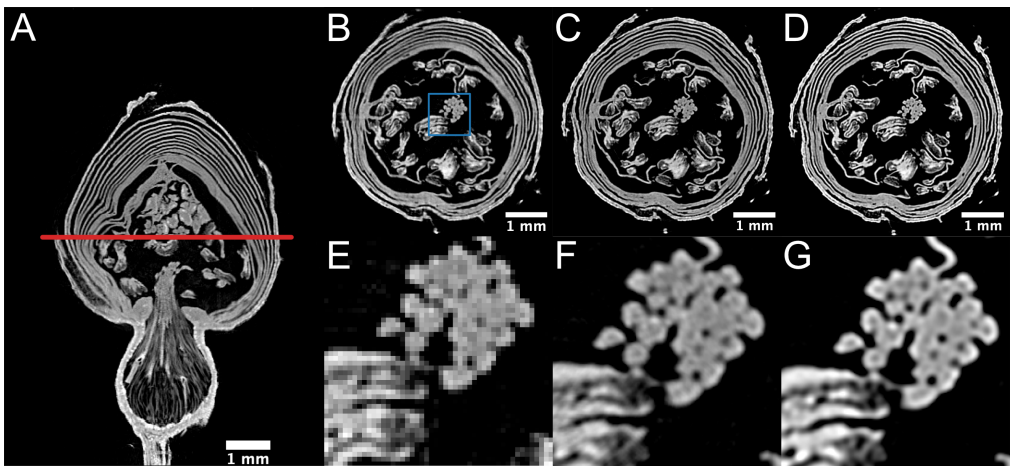

Figure 4.7: Visual evaluation of reconstructed sliced from standard CT, upscaled CT, and super-resolution CT using a dried rose bud in high-magnification geometry. **(A)** Orthogonal slice through the centre of the rosebud. The red line indicates the inspected slice. **(B)** Standard CT. **(C)** Upscaled CT. **(D)** Super-resolution CT. **(E)** Zoom in on the area marked in blue in (B). **(F)** Zoom in corresponding to (C). **(G)** Zoom in corresponding to (D).

Evaluating the different reconstructions visually, as shown for a dried rose bud scanned at high magnification in Figure 4.7, shows a clear improvement of the resolution of small features (Figure 4.7F,G). Upscaling during the reconstruction (Figure 4.7C,F) shows a significant improvement over a regular reconstruction (Figure 4.7B,E) utilising the same data. Comparing to super-resolution (Figure 4.7D,G), which uses significantly more data, shows an even more significant improvement. The edges of features appear sharper and features in general exhibit better contrast and lower noise, which is expected due to the longer total exposure time.

Comparing the different reconstructions showed that both, upscaling and super-resolution, can significantly improve the resolution compared to a standard reconstruction (Figure 4.8). Super-resolution shows the best performance at the cost of a

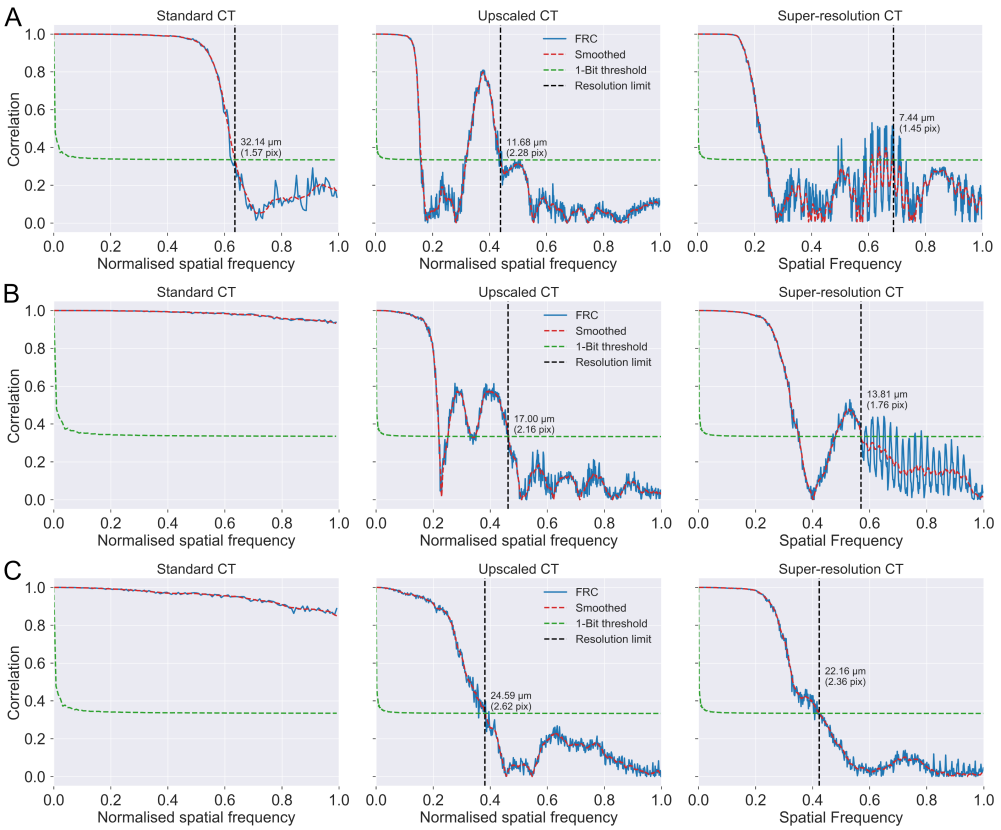

Figure 4.8: Standard CT, upscaled CT, and super-resolution CT evaluated with FRC using a dried rose bud. **(A)** Sample placed at high magnification with 20.54 µm voxel size and 4× upscaling or super-resolution reducing the voxel size to 5.11 µm. **(B)** sample placed at low magnification with 47.18 µm voxel size and 6× upscaling or super-resolution reducing the voxel size to 7.86 µm. **(C)** Sampled placed at low magnification, imaged with the Lambda detector, with a voxel size of 37.5 µm and 4× upscaling or super-resolution reducing the voxel size to 9.375 µm.

significantly longer total measurement time. Evaluating the FRC curves from the scans at low magnification confirmed that the limiting factor is p_{eff} (Figure 4.8B-C), while the limiting factor at high magnification, considering the standard CT reconstruction, can most likely be attributed to penumbral blurring (Figure 4.8A). However, the effect of penumbral blurring could not be observed when using the ESF to evaluate the resolution in high magnification geometry. Instead, the resolution was found to be limited by p_{eff}, which was not expected considering the expected effect of penumbral blurring, as indicated in Figure 4.6B.

While the evaluations of 2D super-resolution in Papers I and II described in Chapters 4.1.2 and 4.1.3 have shown that larger shifts between the low-resolution images are beneficial for the CNR of the estimated super-resolution image, the experiments performed for Paper III showed a potential advantage of limiting the total shift of the

low-resolution images to a single pixel. Scans performed at both geometries (Figure 4.8A-B) using shifts of more than 1 pixel in total, exhibit an oscillation of the FRC at higher frequencies. This could be avoided by limiting the total shift of the images to a single pixel (Figure 4.8C). This effect may be connected to slight differences in the response of individual pixels.

Simply performing a spline interpolation of the projections before reconstruction has also shown an increase in resolution (see Paper III). However, the increase is less significant than performing the upscaling as part of the reconstruction. Interpolating reconstructed slices showed no improvement of the resolution. Generally, super-resolution and upscaling during the reconstruction have both shown significant resolution improvements. Particularly the upscaling approach has shown promise due to its simplicity and the fact that it does not require additional data nor shifts. While super-resolution performs better, a key fragility is the precision of low-resolution image alignment. Small imperfections or sample drifts during the scan can have potentially significant effects on the resulting reconstruction.

4.2 Material decomposition in low-energy micro-CT using an energy-discriminating detector

Obtaining material information to identify or separate different elements through image acquisition with different spectra has been used in clinical imaging for many years [Alvarez and Macovski (1976); Lehmann et al. (1981); Kappadath and Shaw (2004)]. While these methods utilise multiple acquisitions with different spectra, e.g. from a second x-ray source, changing the acceleration voltage of the x-ray source, or applying a filter to the x-ray beam, photon counting detectors with multiple energy-discriminating thresholds can achieve this without changing the x-ray source as demonstrated by Shikhaliev and Fritz (2011); Bateman et al. (2018); Riederer et al. (2019); Marfo et al. (2021). Images containing only photons in a specific energy range are created by subtracting the image obtained at a higher threshold from the image acquired at a lower threshold, as described in Chapter 2.5.4, and are referred to as *energy windows*. The energy dependence of the linear attenuation coefficient μ is exploited, specifically to identify elements with absorption edges [Alvarez and Macovski (1976); Roessl and Proksa (2007); Wang et al. (2009)], as shown in Figure 2.12, allowing to identify specific elements and to decompose the volume into material fractions of a set of different materials.

By acquiring CT scans with energy windows directly below and above an absorption edge of a specific material, the reconstructed slices can be decomposed into three materials, as discussed in Chapter 2.5.4. Generally, one more material than energy windows can be decomposed, i.e. the number of decomposed materials depends on the number of energy bins. The decomposition follows the method outlined by Badea et al. (2012) and is detailed in Paper IV. Basically, the attenuation coefficient in each voxel is expressed as a combination of material specific attenuation coefficients and their fraction. Hence, the decomposition can be performed via a matrix multiplication. Results are improved visually by enforcing a non-negativity constraint as also described by Badea et al. (2012).

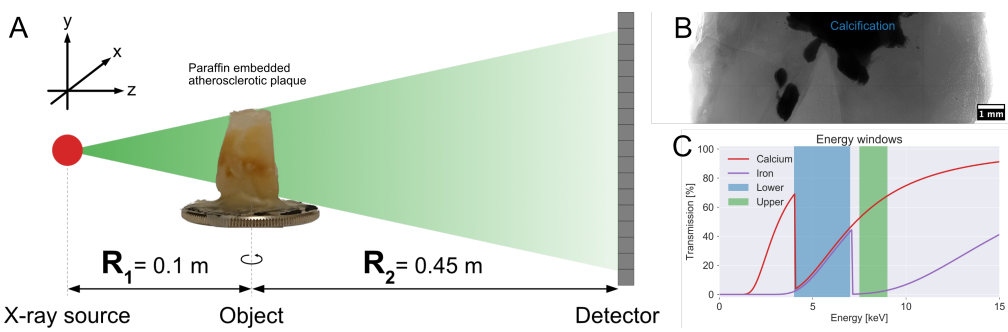

Figure 4.9: Setup and parameter overview. **(A)** Sketch of the used setup with a paraffin embedded atherosclerotic plaque placed 13.6 µm from the source. **(B)** Projection image showing several larger dense calcifications (black) and tissue embedded in paraffin. **(C)** Selected energy windows for the shown plaque samples with the x-ray transmission of the elements of interest. Transmission data simulated for 20 µm of Calcium and Iron using data from Henke et al. (1993).

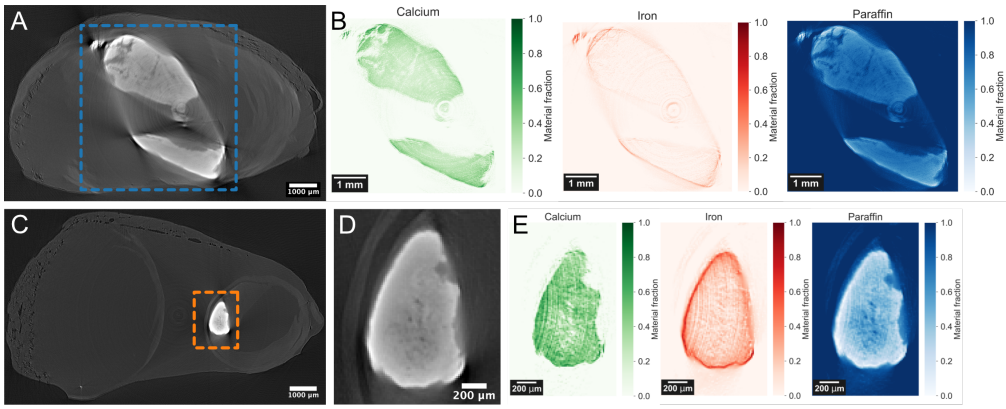

Figure 4.10: Material decomposition of two reconstructed slices from a human atherosclerotic plaque using two energy windows to decompose the scan into Calcium, Iron, and paraffin/tissue/air. **(A)** Reconstructed slice showing two large calcifications. **(B)** Decomposition of the marked area in (A). **(C)** Reconstructed slice showing a smaller calcification. **(D)** Zoom in on the calcification in (C). **(E)** Decomposition of the zoomed in area in (D). *Images adapted from Paper* IV.

The used Eiger detector allows to set thresholds in the range 4 – 11 keV, which gives access to many elements with an atomic number $Z \leq 36$ that occur naturally in biological tissue: Cr, Mn, Fe, Co, Ni, Cu, and Zn. To be able to detect any variations from the absorption edges, the object has to be sufficiently small and low absorbing with the energy ranges as narrow as possible. In this study, the absorption edge of Fe at 7.112 keV has been used as shown in Figure 4.9C, e.g. contained in blood.

In this study, paraffin embedded human atherosclerotic plaques were used. These plaques are a build up of calcium as part of an inflammatory process involving the arterial wall of blood vessels and may cause blood clots leading to a stroke [Feigin et al. (2017); Libby et al. (2019)]. In a previous study, the micro-structure of several plaques had been mapped and compared to histology [Truong et al. (2022)]. One of the disadvantages of the x-ray CT scans was that the information in the images was solely based on attenuation and phase contrast. Hence, structures that appear similar in the x-ray slices may be comprised of different elements, which would potentially make a significant difference in the medical evaluation. Material decomposition offers additional information where certain elements can be identified and localised in x-ray CT without having to perform staining and histology. A detailed study on the elemental composition has been performed using synchrotron-based x-ray fluorescence by De La Rosa et al. (Manuscript in preparation).

Experiments summarised here and detailed in Paper IV were carried out using the micro-CT system described in Chapter 3.1 with a 10 µm x-ray spot at 70 kV acceleration voltage, shown in Figure 4.9A. The object was placed at R_1 = 0.1 m with the detector R_2 = 0.45 m away resulting a magnification of M = 5.5 and thus a p_{eff} of 13.6 µm. A 2D projection is shown in Figure 4.9B showing large calcifications in the embedded tissue. Since the used

detector has only two energy thresholds, i.e. one energy window can be acquired at a time, two acquisitions per projection are required using the energy windows shown in Figure 4.9C. The size of the energy windows is set to at least 1.5 keV corresponding to the energy resolution of the detector. Due to the limited energy range and absorption of lower energies in air, only few photons are detected in the energy windows resulting in long exposure times of up to 200 s per projection.

Following the verification of the method using a phantom consisting of aluminum foil and copper wires, two paraffin embedded human atherosclerotic plaques were scanned and decomposed using the K edge of Iron. Energy windows were set to 4 – 7 keV or 5.5 – 7 keV for the lower energy window and 7.5 – 9 keV for the upper energy window. Decomposition into Iron, Calcium, and paraffin was performed and shows the distributions of Calcium and Iron in the larger calcifications as shown in Figure 4.10. The remainder of the tissue, air, and paraffin wax are labelled as paraffin. Improvements to the detector settings were found after publication of Paper IV, which can alleviate the strong ring artefacts present in the reconstructions (Figure 4.10A,C).

The performed experiments have shown that it is feasible to utilise K edges of naturally occurring materials to decompose a CT scan into several materials. Working with lower energies < 12 keV has also presented challenges regarding the data quality: beam hardening can have a significant impact on the data and the narrow energy windows require long exposure times to detect sufficiently many photons. With improvements to the detector, the ring artefacts can potentially be reduced or avoided in future experiments.

4.3 Vessel imaging in lung tissue using radiopaque dyes

Contrast agents are commonly used in medical imaging to increase the contrast of certain anatomical features by introducing highly absorbing agent, typically based on Iodine or Gadolinium. In biomedical research, where high resolution and satisfactory soft tissue contrast is required, conventional contrast agents typically are too absorbing resulting in artefacts or loss of contrast around the anatomical features affected by the contrast agent. This can be described as *glowing*, obfuscating the areas surrounding the contrast agent. Hence, contrast agents with sufficiently similar attenuation to soft tissue are required. A variety of alternative contrast agents have been developed for different types of micro- or nano-CT and phase contrast imaging, such as using CO_2 injected into vessels [Lundström et al. (2012a,b)] or agents made for specific acquisition and contrast schemes [Lakin et al. (2016); Schaeper et al. (2022); Kuo et al. (2022); Reichmann et al. (2022)].

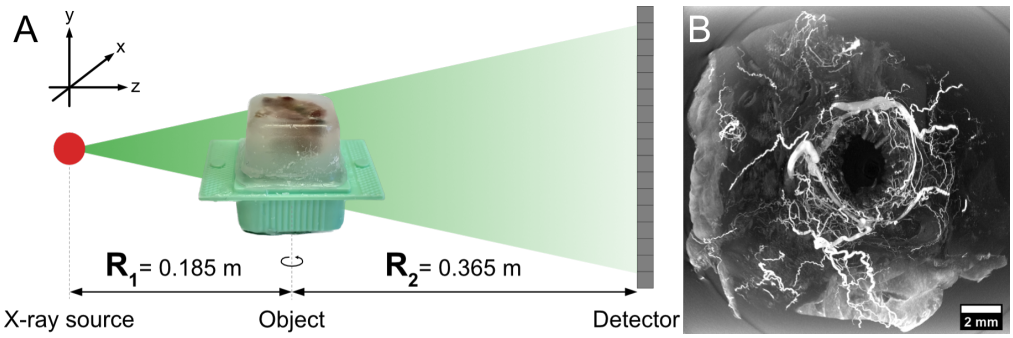

Figure 4.11: (A) Setup sketch with a piece of lung tissue embedded in a $20 \times 20 \times 20$ mm^3 paraffin block on a plastic carrier. **(B)** Maximum intensity projection of a reconstructed volume showing all the dye-filled vessels in the tissue as white.

In Paper V, we investigated tissue marking dyes to identify blood vessels in phase contrast micro-CT of paraffin embedded lung tissue. This project is connected to the study of Pumonary Arterial Hypertension (PAH), a lethal condition leading to remodelling and obstruction of pulmonary arteries carrying deoxygenated blood from the right side of the heart to the lungs. This condition leads to high blood pressure in the affected vessels and progressive right heart failure [Humbert et al. (2019); Galambos et al. (2016)]. Thus, to study PAH, the affected vessels have to be identified and studied in 3D, which is an ongoing research project in the group of Karin Tran-Lundmark (Vessel Wall Biology, Lund University) using synchrotron radiation phase contrast micro-CT [Norvik et al. (2020); Westöö et al. (2021); van der Have et al. (2022)]. In this project, different dye solutions have been evaluated with the aim to achieve sufficient contrast difference between the dye and the tissue, while not causing any artefacts. Additionally, we evaluated if the dyes can be distinguished from each other, to be able to identify different vessels in reconstructed volumes. Since scans, at the synchrotron and in the laboratory, are performed only on parts of the full tissue, filling them with dye before slicing and

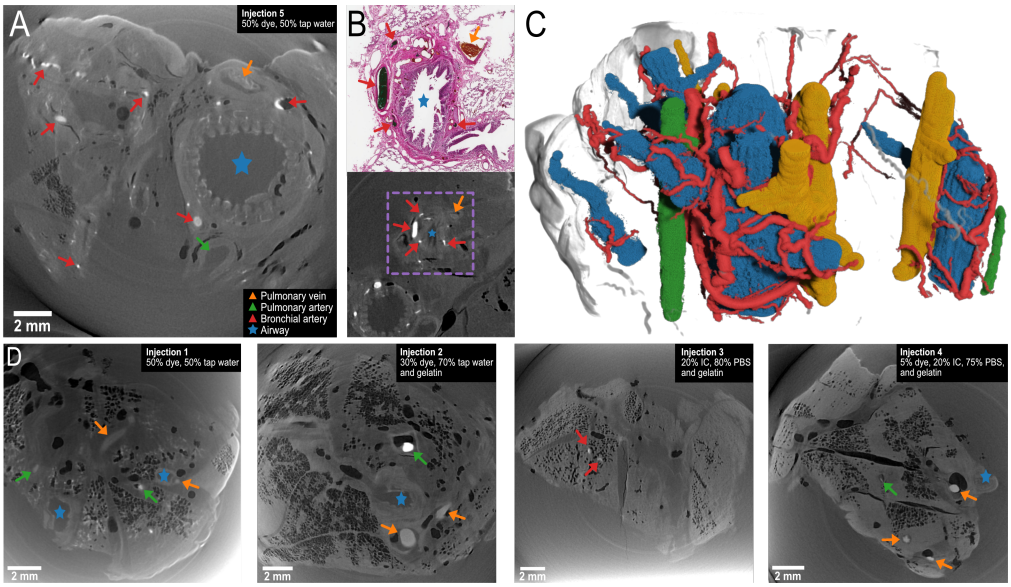

Figure 4.12: Micro-CT of cow lungs. **(A)** Reconstructed slice with bronchial arteries filled with green dye marked red, pulmonary veins filled with yellow dye marked orange, pulmonary arteries without dye marked green, and an airway marked blue. **(B)** Histological section with corresponding area from a micro-CT slice. **(C)** 3D render of the different vessels and airways. **(D)** Reconstructed slices of samples injected with the remaining different dye solutions. *Images adapted from Paper* V.

embedding the tissue into paraffin, allows to easily identify specific vessels. The experiments were performed using bovine lungs since cows have been shown to be particularly susceptible to pulmonary hypertension when housed at high altitudes [Stenmark et al. (1987); Krafsur et al. (2019)] and hence show promise as models to study PAH. For this project, a lung from a healthy cow was used to also function as a control for subsequent studies. Pulmonary veins were filled with yellow dye (orange arrows) and either pulmonary arteries (green arrows) or bronchial arteries (red arrows) were filled with green dye.

The experiments were performed using the micro-CT system described in Chapter 3.1 with the Eiger detector placed 0.55 m from the source. To cover the full width of the paraffin embedded tissue, the object was placed at $R_1 = 0.185$ m resulting in $p_{\text{eff}} = 25.23$ µm, as shown in Figure 4.11A. Hence, a FOV of about 26×7.8 mm^2 was covered. Figure 4.11B shows a maximum intensity projection through a reconstructed volume bringing out all dye filled vessels in the tissue as white. Scans were performed with a x-ray spot size of 10 µm at 70 kV acceleration voltage with 15 W emission power using 3 s exposure time and acquiring 1200 projections. Reconstructions and phase retrieval were performed as described in Chapter 3.1. Segmentation and visualisation of the data were prepared using Dragonfly (Object Research Systems, Canada).

Inspecting a reconstructed slice, as shown in Figure 4.12A, demonstrates that the different dye solutions can be identified in the tissue while no beam hardening or stripe artefacts can be observed. Respective slices for the different dye solutions used are shown in Figure 4.12D. The reconstructed slices also show a key challenge when working with lung tissue: air trapped in the tissue and paraffin wax, manifested as dark areas in the reconstructed slices (Figure 4.12A,D). All tested combinations of dye diluted with tap water and an iodine-based contrast agent diluted with Phosphate-Buffered Saline (PBS) could be identified in the tissue and segmented in 3D. To confirm that a difference in attenuation is related to different colours, some reconstructed slices were compared to equivalent histology slices (Figure 4.12B). Samples where an iodine-based contrast agent was used show significantly less attenuation than expected. One possible explanation is that the contrast did not stay in the vessels and may have leaked or dissipated in the tissue. Further, it has been verified that the dye solutions can be tracked through the scanned volume, shown in Figure 4.12C, by performing 3D segmentations of some of the scans. It could later be observed, when acquiring higher resolution scans, that also the dye solutions appear to have leaked out and accumulated in small bubbles in the tissue as can be observed in Figure 4.13.

4.4 Nano-CT applications

4.4.1 Bovine lungs

In addition to the work presented in Paper V, biopsy punches were taken from some of the samples and scanned in the nano-CT system described in Chapter 3.2. For the scans, 0.5 mm diameter punches were taken from the paraffin blocks and filled into Kapton tubes. The scans were then performed using the Eiger detector at a distance of 388 mm from the source with the tubes placed 3.3 mm from the source resulting in $p_{\text{eff}} = 640$ nm. Evaluating these scans confirmed that the injected dye has also filled the capillaries (Figure 4.13C), the smallest vessels in the tissue with a diameter of a few µm, and that some of the dye solution appears to have leaked from the vessels and accumulated in the tissue (Figure 4.13A). Like in the micro-CT scans, the dyes could clearly be separated from each other (Figure 4.13A-B). Also, it could be shown that a resolution comparable to synchrotron scans can be achieved, although requiring the scanned tissue to be punctured from the larger tissue blocks.

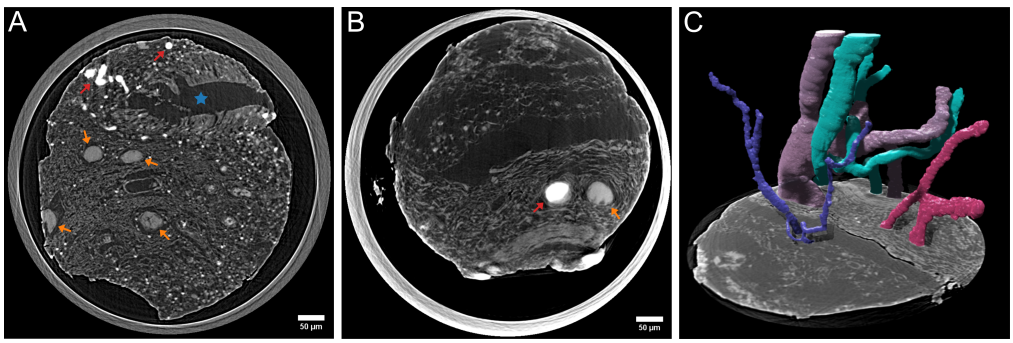

Figure 4.13: Nano-CT scans performed on 0.5 mm biopsy punches of cow lungs with the nano-CT system described in Paper VI and a voxel size of 640 nm. **(A)** Reconstructed slice showing an airway (blue marker) and the two different dyes injected into vessels, marked red and orange. **(B)** Reconstructed slice from a different lung showing different types of tissue and vessels injected with the two different dyes, marked red and orange. **(C)** 3D render of the different vessels corresponding to (B). *Samples provided by Karin Tran-Lundmark, Lund University, and prepared by Gustaf Bernström, Lund University. 3D segmentation and rendering by Sahel Ganji, Lund University.*

4.4.2 Freeze dried leaves

Another application was imaging and characterisation of the internal structure of leaves (Sandèhn et al., manuscript in preparation). 1 mm biopsy punches were taken from freeze dried leaves and scanned with 1.35 µm voxel size (Figure 4.14A-B). Freezer drying was necessary to assure the stability of the sample during the scan. The pores inside the leaves could then be segmented using a watersched algorithm (Figure 4.14C), which allowed to characterise their internal structure. Typical measures are e.g., the sphericity of the pores (Figure 4.14D), i.e. how sphere-like the pores are, and the pore diameters (Figure 4.14E). Techniques like this are valuable for all kinds of research since porous micro-structures are common in all kinds of samples of all length scales.

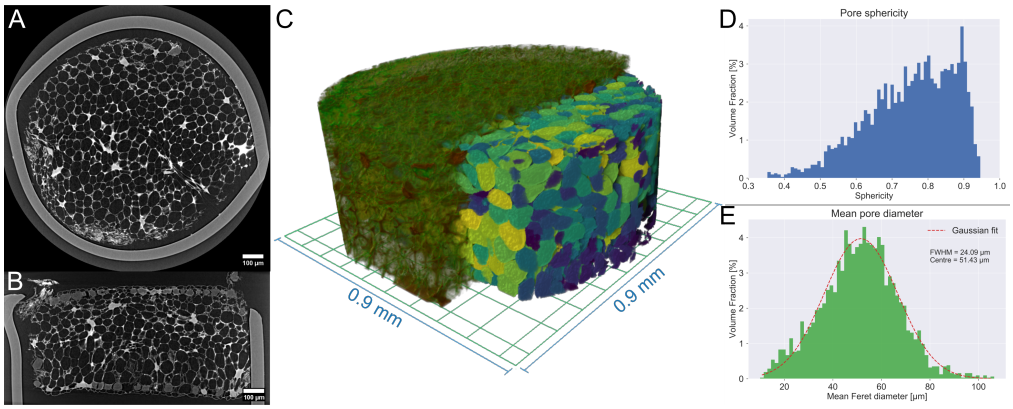

Figure 4.14: High-resolution CT of a 1 mm punch from a freeze dried leaf with 1.35 µm voxel size. **(A)** Reconstructed slice showing the internal porous structure. **(B)** Orthogonal slice through the center of the leaf. **(C)** 3D render of the leaf with the segmented pores coloured based on their sphericity. **(D)** Measured sphericity of the leaf. **(E)** Measured pore diameter using the mean Feret diameter. *Porosity analysis and rendering performed in Dragonfly. Samples provided by Alexandra Sandèhn, Linköping University.*

4.4.3 Mouse hearts

Region-of-interest scans are a common method to achieve high resolution of certain areas in larger samples. While this approach commonly uses detectors with optics, it is still feasible, to some degree, in a magnifying setup. In the imaging of mouse hearts (Peruzzi et al., manuscript in preparation), using paraffin embedded hearts and lungs of mouse fetuses, the heart can be difficult to find in a 2D projection. Hence, overview scans are performed, as shown in Figure 4.15A-B, which are used to identify the region-of-interest for a high-resolution scan (Figure 4.15C).

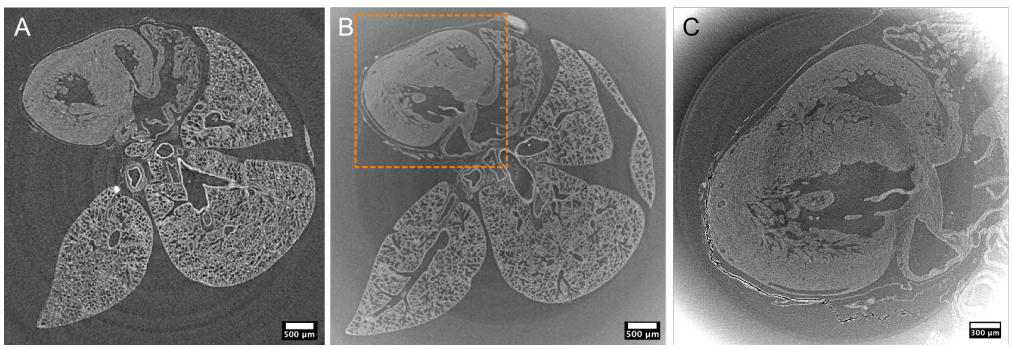

Figure 4.15: High-resolution imaging of a paraffin embedded mouse heart with phase contrast. **(A)** Overview scan using a MetalJet-based micro-CT with a calibrated x-ray spot size of 10 µm and 2.46 µm voxel size using a scintillator-based detector. **(B)** Overview scan from the developed nano-CT system with the Eiger detector and a voxel size of 10.21 µm. **(C)** Region-of-interest scan of the heart (orange area in (B)) with a voxel size of 3.35 µm and a calibrated x-ray spot size of 1.2 µm. *Sample provided by Niccolò Peruzzi, Lund University. Scan in panel (A) by Jenny Romell, Exciscope AB.*

5 Conclusions and outlook

This thesis has introduced a micro- and nano-CT system, their design, implementation, and performance for biomedical imaging. Developments in super-resolution imaging and material decomposition using an energy-discriminating detector have also been demonstrated. The systems have then been used to image tissue and other biomedical samples utilising phase-contrast and achieving micron- and sub-micron resolution.

Super-resolution has shown promise to, effectively, increase the resolution when scanning larger objects that do not fit in the FOV at higher magnification. This approach is, however, still limited by the source size, where the best achievable resolution is about half the FWHM of the x-ray spot, assuming a Gaussian spot shape. The reliability and precision of image registration had the most significant effect on the effectiveness of super-resolution. Hence, for higher resolution systems, where drifts are much more significant, this approach may cause issues. Further, the process to estimate super-resolution projections is computationally expensive and adds the limitations of the chosen interpolation method into the images. Preferable approaches would be to create high-resolution sinograms, as detailed by Yoneyama et al. (2015), or to include the shifted images directly into the reconstruction algorithm and perform the reconstruction onto smaller voxels. However, this approach was not possible when performing the experiments due to a limitation of the number of individual images that could be used for a reconstruction. There may be significant potential for super-resolution in synchrotron applications, particularly in a parallel beam setup as discussed by Sun et al. (2022), where the resolution is defined by the detector and exposure times are quite short. To overcome the main disadvantage of super-resolution: increased total exposure times, using higher flux sources or synchrotrons may make this technique much more usable. Another potential speed up would be to reduce the exposure time of the individual low resolution images.

During this thesis, we have struggled to find suitable applications that require super-resolution. While 2D super-resolution was used as part of the preparation for synchrotron scans by van der Have et al. (2022) and other not yet published experiments, finding an application that requires super-resolution CT has been difficult. The application to lung tissue presented in Paper V has used a smaller spot to leave potential for upscaling, which was not necessary in the end. Similarly, in the imaging of aerogel scaffolds (Oikonomou et al, two manuscripts in preparation), the achieved resolution from a regular CT scan has been found to be sufficient. Regarding the work with medical samples, these are typically prepared in batches, which leaves limited time for scanning before scheduled synchrotron scans and destruction of the samples for histopathological analysis. Hence, the much longer super-resolution scans would likey require too much time. With the implementation of the nano-CT system, much higher resolutions became available, leading to more experiments being conducted at this setup.

Applying super-resolution dark-field imaging, presented in Paper II, has also proven difficult to translate to CT. The used grating was not ideal for this kind of setup, resulting in very low sensitivity. Further, applying super-resolution to the single-shot method has not resulted in particularly consistent results when adding rotation into the setup. Applying the UMPA method [Zdora et al. (2017)] has shown some promise, however, to be viable, the sensitivity has to be improved significantly with a new grating design.

We have demonstrated that material decomposition can be used with tissue samples utilising only naturally occurring elements. While working only with lower energies, in the range of 4 – 11 keV, has had its challenges, it could be shown that it is a feasible approach. The sample size and density are key factors to consider. A too absorbing sample will reduce the effect of the absorption edges to a large degree, making it impossible to detect them. Further, the data presented in Paper IV has suffered from low contrast, high noise, and strong ring artefacts. It has been found out after publication of the paper that these effects could be reduced significantly by changing the detector configuration and optimising the acquisitions. Lastly, beam hardening has been a significant cause of artefacts in the reconstructions, which is amplified due to the limited energy range and the dense calcifications in the used tissue samples.

In the vessel imaging project (Paper V), we have shown that radiopaque dyes can be used to identify and track vessels in lung tissue, without causing artefacts due to their low density. These findings have later also been confirmed using synchrotron imaging. What should be highlighted is the data quality, where a scan time of 1 h produced sufficiently good data to segment the dye filled vessels and identify features in the tissue. As already mentioned before, the time available to scan the tissue samples was limited, hence the comparably short scan times. Following this project, biopsy punches were also scanned in the nano-CT setup. These scans achieved comparable resolution to synchrotron scans typically done on samples like this. Further, the dyes could be tracked down to the smallest vessels in the tissue.

The design and implementation of the nano-CT system was described in Paper VI, discussing the challenges of such systems, like correction of drifts and tilts. Assessing the performance of the system has shown a clear advantage of using photon counting detectors for such systems despite the longer source-detector distance required. The used Eiger detector could achieve resolutions of about $1.25 \times p_{\text{eff}}$, even when applying phase-retrieval, which also gives a significant contrast improvement. Since the achievable resolution relies on geometric magnification, the FOV gets smaller the higher the targeted resolution. Hence, to cover a sufficiently large object at high resolution, a large detector is required, which is the main limitation of this setup at the moment.

Performance of the nano-CT system has also been shown by imaging of freeze dried leaves, allowing to characterise the internal structure. Since the scan times are quite long, the leaves had to be freeze dried to avoid changes of the structure during the scan. Region-of-interest scanning was also shown using a mouse heart. While it is generally preferable

to limit the sample size, it could be shown that also regions inside a larger sample can be imaged at high resolution.

In addition to the imaging techniques and methods investigated in this thesis, the two developed CT systems could, in the future, be applied to more studies and be used to develop new methods expanding the use of x-rays in biomedical research. Extracting additional information with the use of photon counting detectors with multiple energy thresholds is a promising approach for future studies. Further, with new grating designs, dark-field imaging may become a viable option since many biological samples contain scattering structures.

6 Acknowledgements

There have been many people involved who have made this thesis possible, I would like to express my gratitude to all of them.

First and foremost, I would like to express my sincere gratitude to my supervisor Martin, for his guidance, support, and encouragement throughout this PhD. Thank you for you valuable insights and for involving me in many different interesting projects. I would also like to thank my co-supervisors, Ulf and Daniel, for their encouragement and valuable contributions.

I would like to thank the current and previous members of the x-ray phase contrast group: Niccolò, Nathaly, Robin, Sahel, Julia, Rasmus, and Ivan. Thank you for your contributions, encouragement, the lunch and coffee breaks, and afterworks. I would also like to express my gratitude to the Excillum team, particularly: Björn and Lars for the constant supply of (non-thesis related) projects; Tomi, Daniel L, Per, Leland, Andrii, Fei, Björn S, Johan K, Johan N for your all your technical help; Emil, Geethanjali, Shiho, Simona, and Anasuya for taking me to so many intersting conferences and workshops; and the students I got to co-supervise: Aimée, Sara, and Giacomo.

This work would not have been possible without our collaborators. I would like to thank Hanna, Yuhe, Pablo, and Jesper from the synchrotron light division at Lund University for their input, the interesting discussions, and shared beamtimes. Additionally, I'd like to thank the plaque team: Isabel, My, Anneli, Ana, and Lena; and the vessel wall team: Karin, Oscar, Christian N, Christian W, Gustaf, Elna, Ceren, for the interesting shared beamtimes, often conveniently scheduled during weekends. I am also grateful to the electronic plants group at Linköping University: Vasilis, Alexandra, Miriam, Daniela, and Eleni. We have turned a *quick* test into three (at the point of writing this) larger research projects. Also, I would like to thank Jakob, Vedrana, and Anders from QIM for the great collaboration. I would also like to express my gratitude to Jason and Simo from the FLOW lab at UC Berkeley for the great collaboration and company. Finally, I like to acknowledge the beamline staff at NanoMAX: Sebastian, Ulf, Simone, and Maik; at ForMAX: Sam, Kim, Emanuel, Vahid, and Christian; and at TOMCAT: Anne and Goran, for hosting and supporting us many times during the last five years. I would also like to acknowledge Tilman, Spyros, Sascha, and Rizalina from Dectris for all their help during these years.

A special thanks also goes to the colleagues at Medical Radiation Physics, particularly to Ronnie for keeping this project on track, and my fellow PhD students. Finally, I would like to thank my friends and family for their support during these busy years.

List of abbreviations

Ag Silver
BAC Bronnikov Aided Correction
CCD Charged Coupled Device
CdTe Cadmium Telluride
CNR Contrast-to-Noise Ratio
Co Cobalt
Cr Chromium
CsI Caesium Iodine
CT Computed Tomography
Cu Copper
ESF Edge-Spread Function
ESRF European Synchrotron Radiation Facility
FBP Filtered Back-Projection
FDK Feldkamp-Davis-Kress
Fe Iron
FOV Field-of-View
FRC Fourier Ring Correlation
FSC Fourier Shell Correlation
FWHM Full Width at Half Maximum
Ga Gallium
GaAs Gallium Arsenide
Gadox Gadolinium Oxisulfide
In Indium
JIMA Japan Inspection Instruments Manufacturers Association
LuAG Lutetium Aluminium Garnet
Mn Magnesium
Mo Molybdenum
MTF Modulation Transfer Function
Ni Nickel
PAH Pumonary Arterial Hypertension
PB-PCI Propagation-based Phase Contrast Imaging

PBS Phosphate-Buffered Saline

PSF Point-Spread Function

sCMOS Scientific Complementary Metal-Oxide Semiconductor

Si Silicon

SNR Signal-to-Noise Ratio

ToT Time-over-Threshold

UMPA Unified Modulation Pattern Analysis

W Tungsten

Zn Zinc

References

Alvarez, R. E. and Macovski, A. (1976). Energy-selective reconstructions in X-ray computerised tomography. *Physics in Medicine and Biology*, 21(5):002.

An, S., Krapohl, D., Norlin, B., and Thungström, G. (2020). Full-field X-ray fluorescence imaging with a straight polycapillary X-ray collimator. *Journal of Instrumentation*, 15(12):P12033.

Attix, F. H. (2008). *Introduction to Radiological Physics and Radiation Dosimetry*. John Wiley & Sons.

Attwood, D. and Sakdinawatt, A. (2017). *X-Rays and Extreme Ultraviolet Radiation: Principles and Applications*. Cambridge University Press, 2nd edition.

Badea, C. T., Guo, X., Clark, D., Johnston, S. M., Marshall, C. D., and Piantadosi, C. A. (2012). Dual-energy micro-CT of the rodent lung. *American Journal of Physiology-Lung Cellular and Molecular Physiology*, 302(10):L1088–L1097.

Bateman, C., Knight, D., Brandwacht, B., Mahon, J. M., Healy, J., Panta, R., Aamir, R., Rajendran, K., Moghiseh, M., Ramyar, M., Rundle, D., Bennett, J., de Ruiter, N., Smithies, D., Bell, S., Doesburg, R., Chernoglazov, A., Mandalika, V., Walsh, M., Shamshad, M., Anjomrouz, M., Atharifard, A., Broeke, L. V., Bheesette, S., Kirkbride, T., Anderson, N., Gieseg, S., Woodfield, T., Renaud, P., Butler, A., and Butler, P. (2018). MARS-MD: rejection based image domain material decomposition. *Journal of Instrumentation*, 13(05):P05020.

Bech, M., Tapfer, A., Velroyen, A., Yaroshenko, A., Pauwels, B., Hostens, J., Bruyndonckx, P., Sasov, A., and Pfeiffer, F. (2013). In-vivo dark-field and phase-contrast x-ray imaging. *Scientific Reports*, 3(1):3209.

Beer, A. (1852). Bestimmung der Absorption des rothen Lichts in farbigen Flüssigkeiten. *Annalen der Physik und Chemie*, 162(5):78–88.

Berger, M., Hubbell, J., Seltzer, S., Chang, J., Coursey, J., Sukumar, R., Zucker, D., and Olsen, K. (1998). XCOM: Photon cross sections database. *NIST Standard reference database 8*, 8(87).

Bircher, B. A., Meli, F., Küng, A., and Thalmann, R. (2019). CT geometry determination using individual radiographs of calibrated multi-sphere standards. *Special Issue of e-Journal of Nondestructive Testing*, 24(3):2–8.

Blykers, B. K., Organista, C., Boone, M. N., Kagias, M., Marone, F., Stampanoni, M., Bultreys, T., Cnudde, V., and Aelterman, J. (2021). Tunable X-ray dark-field imaging for sub-resolution feature size quantification in porous media. *Scientific Reports*, 11(1):18446.

Bonse, U. and Hart, M. (1965). AN X-RAY INTERFEROMETER. *Applied Physics Letters*, 6(8):155–156.

Boyle, W. S. and Smith, G. E. (1970). Charge Coupled Semiconductor Devices. *Bell System Technical Journal*, 49(4):587–593.

Bravin, A., Coan, P., and Suortti, P. (2013). X-ray phase-contrast imaging: from pre-clinical applications towards clinics. *Physics in Medicine and Biology*, 58(1):R1–R35.

Burvall, A., Larsson, D. H., Lundström, U., Stig, F., Hallström, S., and Hertz, H. M. (2013). Phase-retrieval methods with applications in composite-material tomography. *Journal of Physics: Conference Series*, 463(1):012015.

Burvall, A., Lundström, U., Takman, P. A. C., Larsson, D. H., and Hertz, H. M. (2011). Phase retrieval in X-ray phase-contrast imaging suitable for tomography. *Optics Express*, 19(11):10359.

Bushberg, J., Seibert, J., Leidholdt Jr., E., and Boone, J. (2013). *The Essential Physics of Medical Imaging,*. Lippincott Wiliams & Wilkins, Philadelphia, PA, 3rd editio edition.

Campbell, M., Heijne, E., Meddeler, G., Pernigotti, E., and Snoeys, W. (1998). A readout chip for a 64×64 pixel matrix with 15-bit single photon counting. *IEEE Transactions on Nuclear Science*, 45(3):751–753.

Christoph, R. and Neumann, H. J. (2018). *X-ray tomography in industrial metrology*. Verlag Moderne Industrie, 3rd edition.

Cloetens, P., Ludwig, W., Baruchel, J., Van Dyck, D., Van Landuyt, J., Guigay, J. P., and Schlenker, M. (1999). Holotomography: Quantitative phase tomography with micrometer resolution using hard synchrotron radiation x rays. *Applied Physics Letters*, 75(19):2912–2914.

De Witte, Y., Boone, M., Vlassenbroeck, J., Dierick, M., Masschaele, B., Van Hoorebeke, L., and Cnudde, V. (2009a). Correcting phase contrast artefacts in X-ray CT imaging. In *2009 IEEE International Symposium on Biomedical Imaging: From Nano to Macro*, pages 574–577. IEEE.

De Witte, Y., Boone, M., Vlassenbroeck, J., Dierick, M., and Van Hoorebeke, L. (2009b). Bronnikov-aided correction for x-ray computed tomography. *Journal of the Optical Society of America A*, 26(4):890.

Donath, T., Brandstetter, S., Cibik, L., Commichau, S., Hofer, P., Krumrey, M., Lüthi, B., Marggraf, S., Müller, P., Schneebeli, M., Schulze-Briese, C., and Wernecke, J. (2013). Characterization of the PILATUS photon-counting pixel detector for X-ray energies from 1.75 keV to 60 keV. *Journal of Physics: Conference Series*, 425(6):062001.

Dong, C., Loy, C. C., He, K., and Tang, X. (2016). Image Super-Resolution Using Deep Convolutional Networks. *IEEE Transactions on Pattern Analysis and Machine Intelligence*, 38(2):295–307.

Dudak, J. and Zemlicka, J. (2022). Multi bin energy-sensitive micro-CT using large area photon-counting detectors Timepix. *Journal of Instrumentation*, 17(01):C01028.

EANM (2016). *Radiation Protection and Dose Optimisation: A Technologist's Guide*. EANM.

Eckermann, M., Töpperwien, M., Robisch, A.-L., van der Meer, F., Stadelmann, C., and Salditt, T. (2020). Phase-contrast x-ray tomography of neuronal tissue at laboratory sources with submicron resolution. *Journal of Medical Imaging*, 7(01):1.

Estribeau, M. and Magnan, P. (2004). Fast MTF measurement of CMOS imagers using ISO 12333 slanted-edge methodology. In Chatard, J.-P. and Dennis, P. N. J., editors, *Detectors and Associated Signal Processing*, volume 5251, pages 243–252, St. Etienne, France. SPIE.

Feigin, V. L., Norrving, B., and Mensah, G. A. (2017). Global Burden of Stroke. *Circulation Research*, 120(3):439–448.

Feldkamp, L., Davis, L. C., and Kress, J. W. (1984). Practical cone-beam algorithm. *Journal of the Optical Society of America A*, 1(6):612.

Fella, C., Dittmann, J., Müller, D., Donath, T., Murer, D., Tuohimaa, T., Sofiienko, A., Zabler, S., and Hanke, R. (2018). Implementation of a Computed Tomography System based on a laboratory-based nanofocus X-ray source. *Microscopy and Microanalysis*, 24(S2):236–237.

Ferstl, S., Metscher, B., Müller, M., Allner, S., Dierolf, M., Busse, M., Achterhold, K., Gleich, B., and Pfeiffer, F. (2018). Laboratory-based X-ray NanoCT Explores Morphology of a Zebrafish Embryo. *Microscopy and Microanalysis*, 24(S2):184–185.

Flenner, S., Hagemann, J., Wittwer, F., Longo, E., Kubec, A., Rothkirch, A., David, C., Müller, M., and Greving, I. (2023). Hard X-ray full-field nanoimaging using a direct photon-counting detector. *Journal of Synchrotron Radiation*, 30(2):1–10.

Fröjdh, E., Norlin, B., Thungström, G., and Fröjdh, C. (2011). X-ray absorption and charge transport in a pixellated CdTe detector with single photon processing readout. *Journal of Instrumentation*, 6(02):P02012.

Frost, E. B. (1896). Experiments on the X-rays. *Science*, 3(59):235–236.

Gabor, D. (1948). A New Microscopic Principle. *Nature*, 161(4098):777–778.

Galambos, C., Sims-Lucas, S., Abman, S. H., and Cool, C. D. (2016). Intrapulmonary Bronchopulmonary Anastomoses and Plexiform Lesions in Idiopathic Pulmonary Arterial Hypertension. *American Journal of Respiratory and Critical Care Medicine*, 193(5):574–576.

Gilman, A., Bailey, D. G., and Marsland, S. R. (2008). Interpolation Models for Image Super-resolution. In *4th IEEE International Symposium on Electronic Design, Test and Applications (delta 2008)*, pages 55–60, Hong Kong. IEEE.

Gomes, M. J. and Manakkal, J. M. (2022). Photon-Counting Detectors in Computed Tomography: A Review. *Journal of Health and Allied Sciences NU*.

Gostick, J., Khan, Z., Tranter, T., Kok, M., Agnaou, M., Sadeghi, M., and Jervis, R. (2019). PoreSpy: A Python Toolkit for Quantitative Analysis of Porous Media Images. *Journal of Open Source Software*, 4(37):1296.

Gouillart, E., Nunez-Iglesias, J., and van der Walt, S. (2016). Analyzing microtomography data with Python and the scikit-image library. *Advanced Structural and Chemical Imaging*, 2(1):18.

Graetz, J. (2021). Auto-calibration of cone beam geometries from arbitrary rotating markers using a vector geometry formulation of projection matrices. *Physics in Medicine & Biology*, 66(7):075013.

Graetz, J., Müller, D., Balles, A., and Fella, C. (2021). Lenseless X-ray nano-tomography down to 150 nm resolution: on the quantification of modulation transfer and focal spot of the lab-based ntCT system. *Journal of Instrumentation*, 16(01):P01034.

Granton, P. V., Pollmann, S. I., Ford, N. L., Drangova, M., and Holdsworth, D. W. (2008). Implementation of dual- and triple-energy cone-beam micro-CT for postreconstruction material decomposition. *Medical Physics*, 35(11):5030–5042.

Guizar-Sicairos, M., Thurman, S. T., and Fienup, J. R. (2008). Efficient subpixel image registration algorithms. *Optics Letters*, 33(2):156.

Gureyev, T. E., Mayo, S. C., Myers, D. E., Nesterets, Y., Paganin, D. M., Pogany, A., Stevenson, A. W., and Wilkins, S. W. (2009). Refracting Röntgen's rays: Propagation-based x-ray phase contrast for biomedical imaging. *Journal of Applied Physics*, 105(10):102005.

Gürsoy, D., Hong, Y. P., He, K., Hujsak, K., Yoo, S., Chen, S., Li, Y., Ge, M., Miller, L. M., Chu, Y. S., De Andrade, V., He, K., Cossairt, O., Katsaggelos, A. K., and Jacobsen, C. (2017). Rapid alignment of nanotomography data using joint iterative reconstruction and reprojection. *Scientific Reports*, 7(1):11818.

Gustschin, A., Riedel, M., Taphorn, K., Petrich, C., Gottwald, W., Noichl, W., Busse, M., Francis, S. E., Beckmann, F., Hammel, J. U., Moosmann, J., Thibault, P., and Herzen, J. (2021). High-resolution and sensitivity bi-directional x-ray phase contrast imaging using 2D Talbot array illuminators. *Optica*, 8(12):1588.

Hannesschläger, C., Revol, V., Plank, B., Salaberger, D., and Kastner, J. (2015). Fibre structure characterisation of injection moulded short fibre-reinforced polymers by X-ray scatter dark field tomography. *Case Studies in Nondestructive Testing and Evaluation*, 3:34–41.

Harmon, K. J., Miao, H., Gomella, A. A., Bennett, E. E., Foster, B. A., Bhandarkar, P., and Wen, H. (2015). Motionless electromagnetic phase stepping versus mechanical phase stepping in x-ray phase-contrast imaging with a compact source. *Physics in Medicine and Biology*, 60(8):3031–3043.

Hemberg, O., Otendal, M., and Hertz, H. M. (2003). Liquid-metal-jet anode electron-impact x-ray source. *Applied Physics Letters*, 83(7):1483–1485.

Hendriksen, A. A., Pelt, D. M., and Batenburg, K. J. (2020). Noise2Inverse: Self-Supervised Deep Convolutional Denoising for Tomography. *IEEE Transactions on Computational Imaging*, 6:1320–1335.

Hendriksen, A. A., Schut, D., Palenstijn, W. J., Viganó, N., Kim, J., Pelt, D. M., van Leeuwen, T., and Joost Batenburg, K. (2021). Tomosipo: fast, flexible, and convenient 3D tomography for complex scanning geometries in Python. *Optics Express*, 29(24):40494.

Henke, B., Gullikson, E., and Davis, J. (1993). X-Ray Interactions: Photoabsorption, Scattering, Transmission, and Reflection at E = 50-30,000 eV, Z = 1-92. *Atomic Data and Nuclear Data Tables*, 54(2):181–342.

Henrich, B., Bergamaschi, A., Broennimann, C., Dinapoli, R., Eikenberry, E., Johnson, I., Kobas, M., Kraft, P., Mozzanica, A., and Schmitt, B. (2009). PILATUS: A single photon counting pixel detector for X-ray applications. *Nuclear Instruments and Methods in Physics Research Section A: Accelerators, Spectrometers, Detectors and Associated Equipment*, 607(1):247–249.

Hounsfield, G. N. (1973). Computerized transverse axial scanning (tomography): Part 1. Description of system. *The British Journal of Radiology*, 46(552):1016–1022.

Humbert, M., Guignabert, C., Bonnet, S., Dorfmüller, P., Klinger, J. R., Nicolls, M. R., Olschewski, A. J., Pullamsetti, S. S., Schermuly, R. T., Stenmark, K. R., and Rabinovitch, M. (2019). Pathology and pathobiology of pulmonary hypertension: state of the art and research perspectives. *European Respiratory Journal*, 53(1):1801887.

Irani, M. and Peleg, S. (1991). Improving resolution by image registration. *CVGIP: Graphical Models and Image Processing*, 53(3):231–239.

Ishitani, T. and Sato, M. (2007). Evaluation of both image resolution and contrast-to-noise ratio in scanning electron microscopy. *Journal of Electron Microscopy*, 56(4):145–151.

Jacobsen, C. (2019). *X-ray Microscopy*. Cambridge University Press.

Jakubek, J., Cejnarova, A., Holy, T., Pospisil, S., Uher, J., and Vykydal, Z. (2008). Pixel detectors for imaging with heavy charged particles. *Nuclear Instruments and Methods in Physics Research Section A: Accelerators, Spectrometers, Detectors and Associated Equipment*, 591(1):155–158.

Johnson, I., Bergamaschi, A., Billich, H., Cartier, S., Dinapoli, R., Greiffenberg, D., Guizar-Sicairos, M., Henrich, B., Jungmann, J., Mezza, D., Mozzanica, A., Schmitt, B., Shi, X., and Tinti, G. (2014). Eiger: a single-photon counting x-ray detector. *Journal of Instrumentation*, 9(05):C05032.

Jørgensen, J. S., Ametova, E., Burca, G., Fardell, G., Papoutsellis, E., Pasca, E., Thielemans, K., Turner, M., Warr, R., Lionheart, W. R. B., and Withers, P. J. (2021). Core Imaging Library - Part I: a versatile Python framework for tomographic imaging. *Philosophical Transactions of the Royal Society A: Mathematical, Physical and Engineering Sciences*, 379(2204):20200192.

Jowitt, L., Wilson, M., Seller, P., Angelsen, C., Wheater, R., Cline, B., Schöne, D., Lauba, F., Goede, M., Ball, R., Verhoeven, M., Gottseleben, G., Boone, M., Van Assche, F., and Veale, M. (2022). HEXITEC 2 × 2 tiled hard X-ray spectroscopic imaging detector system. *Journal of Instrumentation*, 17(01):P01012.

Kak, A. C. and Slaney, M. (2001). Algorithms for Reconstruction with Nondiffracting Sources. In *Principles of Computerized Tomographic Imaging*, chapter 3, pages 49–112. Society for Industrial and Applied Mathematics.

Kappadath, S. C. and Shaw, C. C. (2004). Quantitative evaluation of dual-energy digital mammography for calcification imaging. *Physics in Medicine and Biology*, 49(12):2563–2576.

Kim, E. H., Preissner, M., Carnibella, R. P., Samarage, C. R., Bennett, E., Diniz, M. A., Fouras, A., Zosky, G. R., and Jones, H. D. (2017). Novel analysis of 4DCT imaging quantifies progressive increases in anatomic dead space during mechanical ventilation in mice. *Journal of Applied Physiology*, 123(3):578–584.

Koch, A., Raven, C., Spanne, P., and Snigirev, A. (1998). X-ray imaging with submicrometer resolution employing transparent luminescent screens. *Journal of the Optical Society of America A*, 15(7):1940.

Krafsur, G. M., Neary, J. M., Garry, F., Holt, T., Gould, D. H., Mason, G. L., Thomas, M. G., Enns, R. M., Tuder, R. M., Heaton, M. P., Brown, R. D., and Stenmark, K. R. (2019). Cardiopulmonary remodeling in fattened beef cattle: a naturally occurring large animal model of obesity-associated pulmonary hypertension with left heart disease. *Pulmonary Circulation*, 9(1):1–13.

Krapohl, D. (2015). *Monte Carlo and Charge Transport Simulation of Pixel Detector Systems*. Mid Sweden University, Sundsvall, Sweden.

Kuo, W., Le, N. A., Spingler, B., Schulz, G., Müller, B., and Kurtcuoglu, V. (2022). Tomographic imaging of microvasculature with a purpose-designed, polymeric x-ray contrast agent. In Müller, B. and Wang, G., editors, *Developments in X-Ray Tomography XIV*, volume 12242, San Diego, California. SPIE.

Lakin, B. A., Patel, H., Holland, C., Freedman, J. D., Shelofsky, J. S., Snyder, B. D., Stok, K. S., and Grinstaff, M. W. (2016). Contrast-enhanced CT using a cationic contrast agent enables non-destructive assessment of the biochemical and biomechanical properties of mouse tibial plateau cartilage. *Journal of Orthopaedic Research*, 34(7):1130–1138.

Lalush, D. S. and Wernick, M. N. (2004). Iterative Image Reconstruction. In *Emission Tomography*, chapter 21, pages 443–472. Academic Press, San Diego, California.

Larsson, D. H., Takman, P. A. C., Lundström, U., Burvall, A., and Hertz, H. M. (2011). A 24 keV liquid-metal-jet x-ray source for biomedical applications. *Review of Scientific Instruments*, 82(12):123701.

Larsson, D. H., Vågberg, W., Yaroshenko, A., Yildirim, A. Ö., and Hertz, H. M. (2016). High-resolution short-exposure small-animal laboratory x-ray phase-contrast tomography. *Scientific Reports*, 6(1):39074.

Lehmann, L. A., Alvarez, R. E., Macovski, A., Brody, W. R., Pelc, N. J., Riederer, S. J., and Hall, A. L. (1981). Generalized image combinations in dual KVP digital radiography. *Medical Physics*, 8(5):659–667.

Libby, P., Buring, J. E., Badimon, L., Hansson, G. K., Deanfield, J., Bittencourt, M. S., Tokgözoğlu, L., and Lewis, E. F. (2019). Atherosclerosis. *Nature Reviews Disease Primers*, 5(1):56.

Llopart, X., Ballabriga, R., Campbell, M., Tlustos, L., and Wong, W. (2007). Timepix, a 65k programmable pixel readout chip for arrival time, energy and/or photon counting measurements. *Nuclear Instruments and Methods in Physics Research Section A: Accelerators, Spectrometers, Detectors and Associated Equipment*, 581(1-2):485–494.

Lundström, U., Larsson, D. H., Burvall, A., Scott, L., Westermark, U. K., Wilhelm, M., Arsenian Henriksson, M., and Hertz, H. M. (2012a). X-ray phase-contrast CO 2 angiography for sub-10 μm vessel imaging. *Physics in Medicine and Biology*, 57(22):7431–7441.

Lundström, U., Larsson, D. H., Burvall, A., Takman, P. A. C., Scott, L., Brismar, H., and Hertz, H. M. (2012b). X-ray phase contrast for CO 2 microangiography. *Physics in Medicine and Biology*, 57(9):2603–2617.

Maneuski, D., Astromskas, V., Fröjdh, E., Fröjdh, C., Gimenez, E. N., Marchal, J., O'Shea, V., Stewart, G., Tartoni, N., Wilhelm, H., Wraight, K., and Zain, R. M. (2012). Imaging and spectroscopic performance studies of pixellated CdTe Timepix detector. *Journal of Instrumentation*, 7(01):C01038.

Marfo, E., Anderson, N. G., Butler, A. P. H., Schleich, N., Carbonez, P., Damet, J., Lowe, C., Healy, J., Chernoglazov, A. I., Moghiseh, M., and Raja, A. Y. (2021). Assessment of Material Identification Errors, Image Quality, and Radiation Doses Using Small Animal Spectral Photon-Counting CT. *IEEE Transactions on Radiation and Plasma Medical Sciences*, 5(4):578–587.

Mayerhöfer, T. G., Pahlow, S., and Popp, J. (2020). The Bouguer-Beer-Lambert Law: Shining Light on the Obscure. *ChemPhysChem*, 21(18):2029–2046.

Mayo, S. C., Miller, P. R., Wilkins, S. W., Davis, T. J., Gao, D., Gureyev, T. E., Paganin, D., Parry, D. J., Pogany, A., and Stevenson, A. W. (2002). Quantitative X-ray projection microscopy: phase-contrast and multi-spectral imaging. *Journal of Microscopy*, 207(2):79–96.

Michelson, A. A. (1927). *Studies in optics*. University Press, Chicago, 1st edition.

Micieli, D., Minniti, T., and Gorini, G. (2019). NeuTomPy toolbox, a Python package for tomographic data processing and reconstruction. *SoftwareX*, 9:260–264.

Milanfar, P. (2010). *Super-Resolution Imaging*. CRC Press, Boca Raton, 1st edition.

Momose, A. and Fukuda, J. (1995). Phase-contrast radiographs of nonstained rat cerebellar specimen. *Medical Physics*, 22(4):375–379.

Momose, A., Kawamoto, S., Koyama, I., Hamaishi, Y., Takai, K., and Suzuki, Y. (2003). Demonstration of X-Ray Talbot Interferometry. *Japanese Journal of Applied Physics*, 42(Part 2, No. 7B):L866–L868.

Momose, A., Takeda, T., Itai, Y., and Hirano, K. (1996). Phase–contrast X–ray computed tomography for observing biological soft tissues. *Nature Medicine*, 2(4):473–475.

Morgan, K. S., Paganin, D. M., and Siu, K. K. W. (2012). X-ray phase imaging with a paper analyzer. *Applied Physics Letters*, 100(12):124102.

Müller, D., Fella, C., Altmann, F., Graetz, J., Balles, A., Ring, M., and Gambino, J. (2022). Characterization of electrically stressed power device metallization using nano-CT imaging. *Microelectronics Reliability*, 135(February):114589.

Müller, D., Graetz, J., Balles, A., Stier, S., Hanke, R., and Fella, C. (2021). Laboratory-Based Nano-Computed Tomography and Examples of Its Application in the Field of Materials Research. *Crystals*, 11(6):677.

Müller, M., de Sena Oliveira, I., Allner, S., Ferstl, S., Bidola, P., Mechlem, K., Fehringer, A., Hehn, L., Dierolf, M., Achterhold, K., Gleich, B., Hammel, J. U., Jahn, H., Mayer, G., and Pfeiffer, F. (2017). Myoanatomy of the velvet worm leg revealed by laboratory-based nanofocus X-ray source tomography. *Proceedings of the National Academy of Sciences*, 114(47):12378–12383.

Münch, B., Trtik, P., Marone, F., and Stampanoni, M. (2009). Stripe and ring artifact removal with combined wavelet—Fourier filtering. *Optics Express*, 17(10):8567.

Nachtrab, F., Firsching, M., Uhlmann, N., Speier, C., Takman, P., Tuohimaa, T., Heinzl, C., Kastner, J., Larsson, D. H., Holmberg, A., Berti, G., Krumm, M., and Sauerwein, C. (2014). NanoXCT: development of a laboratory nano-CT system. In Stock, S. R., editor, *Developments in X-Ray Tomography IX*, page 92120L, San Diego, California. SPIE.

Navarrete, C., Procz, S., Fey, J., Roque, G., Avila, C., Schuetz, M., Olivo, A., and Fiederle, M. (2019). Energy sensitive X-ray phase contrast imaging with a CdTe-Timepix3 detector. In *2019 IEEE Nuclear Science Symposium and Medical Imaging Conference (NSS/MIC)*, pages 1–6. IEEE.

Nikitin, V., De Andrade, V., Slyamov, A., Gould, B., Zhang, Y., Sampathkumar, V., Kasthuri, N., Gursoy, D., and De Carlo, F. (2021). Distributed Optimization for Nonrigid Nano-Tomography. *IEEE Transactions on Computational Imaging*, 7:272–287.

Norvik, C., Westöö, C. K., Peruzzi, N., Lovric, G., van der Have, O., Mokso, R., Jeremiasen, I., Brunnström, H., Galambos, C., Bech, M., and Tran-Lundmark, K. (2020). Synchrotron-based phase-contrast micro-CT as a tool for understanding pulmonary vascular pathobiology and the 3-D microanatomy of alveolar capillary dysplasia. *American Journal of Physiology-Lung Cellular and Molecular Physiology*, 318(1):L65–L75.

Olivo, A. and Speller, R. (2007). Modelling of a novel x-ray phase contrast imaging technique based on coded apertures. *Physics in Medicine and Biology*, 52(22):6555–6573.

Paganin, D., Mayo, S. C., Gureyev, T. E., Miller, P. R., and Wilkins, S. W. (2002). Simultaneous phase and amplitude extraction from a single defocused image of a homogeneous object. *Journal of Microscopy*, 206(1):33–40.

Paganin, D. M., Favre-Nicolin, V., Mirone, A., Rack, A., Villanova, J., Olbinado, M. P., Fernandez, V., da Silva, J. C., and Pelliccia, D. (2020). Boosting spatial resolution by incorporating periodic boundary conditions into single-distance hard-x-ray phase retrieval. *Journal of Optics*, 22(11):115607.

Pande, K., Donatelli, J. J., Parkinson, D. Y., Yan, H., and Sethian, J. A. (2022). Joint iterative reconstruction and 3D rigid alignment for X-ray tomography. *Optics Express*, 30(6):8898.

Park, S. C., Park, M. K., and Moon, M. G. (2003). Super-resolution image reconstruction: a technical overview. *IEEE Signal Processing Magazine*, 20(3):21–36.

Peli, E. (1990). Contrast in complex images. *Journal of the Optical Society of America A*, 7(10):2032.

Pennicard, D., Lange, S., Smoljanin, S., Hirsemann, H., and Graafsma, H. (2012). LAMBDA — Large Area Medipix3-Based Detector Array. *Journal of Instrumentation*, 7(11):C11009.

Peruzzi, N., Veress, B., Dahlin, L. B., Salditt, T., Andersson, M., Eckermann, M., Frohn, J., Robisch, A.-L., Bech, M., and Ohlsson, B. (2020). 3D analysis of the myenteric plexus of the human bowel by X-ray phase-contrast tomography – a future method? *Scandinavian Journal of Gastroenterology*, 55(10):1261–1267.

Pfeiffer, F. (2018). X-ray ptychography. *Nature Photonics*, 12(1):9–17.

Pfeiffer, F., Bech, M., Bunk, O., Kraft, P., Eikenberry, E. F., Brönnimann, C., Grünzweig, C., and David, C. (2008). Hard-X-ray dark-field imaging using a grating interferometer. *Nature Materials*, 7(2):134–137.

Pfeiffer, F., Herzen, J., Willner, M., Chabior, M., Auweter, S., Reiser, M., and Bamberg, F. (2013). Grating-based X-ray phase contrast for biomedical imaging applications. *Zeitschrift fur Medizinische Physik*, 23(3):176–185.

Pfeiffer, F., Weitkamp, T., Bunk, O., and David, C. (2006). Phase retrieval and differential phase-contrast imaging with low-brilliance X-ray sources. *Nature Physics*, 2(4):258–261.

Podgoršak, E. B. (2009). Production of X Rays. In *Radiation Physics for Medical Physicists*, chapter 4, pages 177–205. Springer, Berlin/Heidelberg, 2nd edition.

Quenot, L., Bohic, S., and Brun, E. (2022). X-ray Phase Contrast Imaging from Synchrotron to Conventional Sources: A Review of the Existing Techniques for Biological Applications. *Applied Sciences*, 12(19):9539.

Radon, J. (1986). On the determination of functions from their integral values along certain manifolds. *IEEE Transactions on Medical Imaging*, 5(4):170–176.

Reichmann, J., Ruhwedel, T., Möbius, W., and Salditt, T. (2022). Neodymium acetate as a contrast agent for x-ray phase-contrast tomography. In Müller, B. and Wang, G., editors, *Developments in X-Ray Tomography XIV*, volume 12242, San Diego, California. SPIE.

Riederer, I., Si-Mohamed, S., Ehn, S., Bar-Ness, D., Noël, P. B., Fingerle, A. A., Pfeiffer, F., Rummeny, E. J., Douek, P., and Pfeiffer, D. (2019). Differentiation between blood and iodine in a bovine brain—Initial experience with Spectral Photon-Counting Computed Tomography (SPCCT). *PLoS ONE*, 14(2):e0212679.

Roessl, E. and Proksa, R. (2007). K-edge imaging in x-ray computed tomography using multi-bin photon counting detectors. *Physics in Medicine and Biology*, 52(15):4679–4696.

Romell, J., Jie, V. W., Miettinen, A., Baird, E., and Hertz, H. M. (2021). Laboratory phase-contrast nanotomography of unstained Bombus terrestris compound eyes. *Journal of Microscopy*, 283(1):29–40.

Röntgen, W. C. (1898). Über eine neue Art von Strahlen. *Annalen der Physik*, 300(1):12–17.

Rossi, L., Fischer, P., Rohe, T., and Wermes, N. (2006). *Pixel Detectors*. Particle Acceleration and Detection. Springer, Berlin, Heidelberg.

Samber, B. D., Renders, J., Elberfeld, T., Maris, Y., Sanctorum, J., Six, N., Liang, Z., Beenhouwer, J. D., and Sijbers, J. (2021). FleXCT: a flexible X-ray CT scanner with 10 degrees of freedom. *Optics Express*, 29(3):3438.

Schaeper, J. J., Liberman, M. C., and Salditt, T. (2022). Imaging of excised cochleae by micro-CT: staining, liquid embedding, and image modalities. In Müller, B. and Wang, G., editors, *Developments in X-Ray Tomography XIV*, volume 12242, San Diego, California. SPIE.

Schindelin, J., Arganda-Carreras, I., Frise, E., Kaynig, V., Longair, M., Pietzsch, T., Preibisch, S., Rueden, C., Saalfeld, S., Schmid, B., Tinevez, J.-Y., White, D. J., Hartenstein, V., Eliceiri, K., Tomancak, P., and Cardona, A. (2012). Fiji: an open-source platform for biological-image analysis. *Nature Methods*, 9(7):676–682.

Scholz, J., Birnbacher, L., Petrich, C., Riedel, M., Heck, L., Gkoumas, S., Sellerer, T., Achterhold, K., and Herzen, J. (2020). Biomedical x-ray imaging with a GaAs photon-counting detector: A comparative study. *APL Photonics*, 5(10):106108.

Schulz, G., Weitkamp, T., Zanette, I., Pfeiffer, F., Beckmann, F., David, C., Rutishauser, S., Reznikova, E., and Müller, B. (2010). High-resolution tomographic imaging of a human cerebellum: comparison of absorption and grating-based phase contrast. *Journal of The Royal Society Interface*, 7(53):1665–1676.

Sheppard, A. P., Sok, R. M., and Averdunk, H. (2004). Techniques for image enhancement and segmentation of tomographic images of porous materials. *Physica A: Statistical Mechanics and its Applications*, 339(1-2):145–151.

Shikhaliev, P. M. and Fritz, S. G. (2011). Photon counting spectral CT versus conventional CT: comparative evaluation for breast imaging application. *Physics in Medicine and Biology*, 56(7):1905–1930.

Snigirev, A., Snigireva, I., Kohn, V., Kuznetsov, S., and Schelokov, I. (1995). On the possibilities of x-ray phase contrast microimaging by coherent high-energy synchrotron radiation. *Review of Scientific Instruments*, 66(12):5486–5492.

Sroubek, F., Cristobal, G., and Flusser, J. (2007). A Unified Approach to Superresolution and Multichannel Blind Deconvolution. *IEEE Transactions on Image Processing*, 16(9):2322–2332.

Sroubek, F. and Flusser, J. (2005). Multichannel blind deconvolution of spatially misaligned images. *IEEE Transactions on Image Processing*, 14(7):874–883.

Sroubek, F., Flusser, J., and Cristóbal, G. (2017). *Blind Image Deconvolution*. CRC Press.

Sroubek, F. and Milanfar, P. (2012). Robust Multichannel Blind Deconvolution via Fast Alternating Minimization. *IEEE Transactions on Image Processing*, 21(4):1687–1700.

Stampanoni, M., Wang, Z., Thüring, T., David, C., Roessl, E., Trippel, M., Kubik-Huch, R. A., Singer, G., Hohl, M. K., and Hauser, N. (2011). The First Analysis and Clinical Evaluation of Native Breast Tissue Using Differential Phase-Contrast Mammography. *Investigative Radiology*, 46(12):801–806.

Stenmark, K. R., Fasules, J., Hyde, D. M., Voelkel, N. F., Henson, J., Tucker, A., Wilson, H., and Reeves, J. T. (1987). Severe pulmonary hypertension and arterial adventitial changes in newborn calves at 4,300 m. *Journal of Applied Physiology*, 62(2):821–830.

Sun, R., Wang, Y., Zhang, J., Deng, T., Yi, Q., Yu, B., Huang, M., Li, G., and Jiang, X. (2022). Synchrotron radiation X-ray imaging with large field of view and high resolution using micro-scanning method. *Journal of Synchrotron Radiation*, 29(5):1241–1250.

Taguchi, K. and Iwanczyk, J. S. (2013). Vision 20/20: Single photon counting x-ray detectors in medical imaging. *Medical Physics*, 40(10):100901.

Tapfer, A., Bech, M., Pauwels, B., Liu, X., Bruyndonckx, P., Sasov, A., Kenntner, J., Mohr, J., Walter, M., Schulz, J., and Pfeiffer, F. (2011). SU-C-211-01: First Results from a Preclinical X-Ray Phase-Contrast CT Scanner. *Medical Physics*, 38(6):3375.

Tapfer, A., Bech, M., Velroyen, A., Meiser, J., Mohr, J., Walter, M., Schulz, J., Pauwels, B., Bruyndonckx, P., Liu, X., Sasov, A., and Pfeiffer, F. (2012). Experimental results from a preclinical X-ray phase-contrast CT scanner. *Proceedings of the National Academy of Sciences*, 109(39):15691–15696.

Thibault, P., Dierolf, M., Menzel, A., Bunk, O., David, C., and Pfeiffer, F. (2008). High-Resolution Scanning X-ray Diffraction Microscopy. *Science*, 321(5887):379–382.

Töpperwien, M., Krenkel, M., Vincenz, D., Stöber, F., Oelschlegel, A. M., Goldschmidt, J., and Salditt, T. (2017). Three-dimensional mouse brain cytoarchitecture revealed by laboratory-based x-ray phase-contrast tomography. *Scientific Reports*, 7(1):42847.

Truong, M., Dreier, T., Wassélius, J., Sundius, L., Persson, A., Lovric, G., Bonnin, A., Goncalves, I., and Bech, M. (2022). Sub-micrometer morphology of human atherosclerotic plaque revealed by synchrotron radiation-based μCT—A comparison with histology. *PLoS ONE*, 17(4):e0265598.

Tsui, B. M. W. and Frey, E. C. (2006). Analytic Image Reconstruction Methods in Emission Computed Tomography. In Zaidi, H., editor, *Quantitative Analysis in Nuclear Medicine Imaging*, chapter 3, pages 82–106. Springer US, Boston, MA.

Tuohimaa, T., Otendal, M., and Hertz, H. M. (2007). Phase-contrast x-ray imaging with a liquid-metal-jet-anode microfocus source. *Applied Physics Letters*, 91(7):074104.

Vågberg, W., Persson, J., Szekely, L., and Hertz, H. M. (2018). Cellular-resolution 3D virtual histology of human coronary arteries using x-ray phase tomography. *Scientific Reports*, 8(1):11014.

van Aarle, W., Palenstijn, W. J., Cant, J., Janssens, E., Bleichrodt, F., Dabravolski, A., De Beenhouwer, J., Joost Batenburg, K., and Sijbers, J. (2016). Fast and flexible X-ray tomography using the ASTRA toolbox. *Optics Express*, 24(22):25129–25148.

van Aarle, W., Palenstijn, W. J., De Beenhouwer, J., Altantzis, T., Bals, S., Batenburg, K. J., and Sijbers, J. (2015). The ASTRA Toolbox: A platform for advanced algorithm development in electron tomography. *Ultramicroscopy*, 157(2015):35–47.

van der Have, O., Westöö, C., Ahrné, F., Tian, X., Ichimura, K., Dreier, T., Norvik, C., Kumar, M. E., Spiekerkoetter, E., and Tran-Lundmark, K. (2022). Shunt-type

plexiform lesions identified in the Sugen5416/hypoxia rat model of pulmonary arterial hypertension using synchrotron-based phase-contrast micro-CT. *European Respiratory Journal*, 59(6):2102802.

van Heel, M. (1987). Similarity measures between images. *Ultramicroscopy*, 21(1):95–100.

van Heel, M. and Schatz, M. (2005). Fourier shell correlation threshold criteria. *Journal of Structural Biology*, 151(3):250–262.

Vavřík, D., Jakůbek, J., Kumpova, I., and Pichotka, M. (2017). Laboratory based study of dynamical processes by 4D X-ray CT with sub-second temporal resolution. *Journal of Instrumentation*, 12(02):C02010.

Viermetz, M., Gustschin, N., Schmid, C., Haeusele, J., von Teuffenbach, M., Meyer, P., Bergner, F., Lasser, T., Proksa, R., Koehler, T., and Pfeiffer, F. (2022). Dark-field computed tomography reaches the human scale. *Proceedings of the National Academy of Sciences*, 119(8):e2118799119.

Vo, N. T., Atwood, R. C., and Drakopoulos, M. (2018). Superior techniques for eliminating ring artifacts in X-ray micro-tomography. *Optics Express*, 26(22):28396.

Vo, N. T., Atwood, R. C., Drakopoulos, M., and Connolley, T. (2021). Data processing methods and data acquisition for samples larger than the field of view in parallel-beam tomography. *Optics Express*, 29(12):17849.

Wang, Z., Huang, Z., Zhang, L., Kang, K., and Zhu, P. (2009). Fast X-Ray Phase-Contrast Imaging Using High Resolution Detector. *IEEE Transactions on Nuclear Science*, 56(3):1383–1388.

Weitkamp, T., Diaz, A., David, C., Pfeiffer, F., Stampanoni, M., Cloetens, P., and Ziegler, E. (2005). X-ray phase imaging with a grating interferometer. *Optics Express*, 13(16):6296.

Wen, H., Bennett, E., Hegedus, M., and Carroll, S. (2008). Spatial Harmonic Imaging of X-ray Scattering—Initial Results. *IEEE Transactions on Medical Imaging*, 27(8):997–1002.

Wen, H. H., Bennett, E. E., Kopace, R., Stein, A. F., and Pai, V. (2010). Single-shot x-ray differential phase-contrast and diffraction imaging using two-dimensional transmission gratings. *Optics Letters*, 35(12):1932.

Westöö, C., Norvik, C., Peruzzi, N., van der Have, O., Lovric, G., Jeremiasen, I., Tran, P.-K., Mokso, R., de Jesus Perez, V., Brunnström, H., Bech, M., Galambos, C., and Tran-Lundmark, K. (2021). Distinct types of plexiform lesions identified by synchrotron-based phase-contrast micro-CT. *American Journal of Physiology-Lung Cellular and Molecular Physiology*, 321(1):L17–L28.

Wilkins, S. W., Gureyev, T. E., Gao, D., Pogany, A., and Stevenson, A. W. (1996). Phase-contrast imaging using polychromatic hard X-rays. *Nature*, 384(6607):335–338.

Willer, K., Fingerle, A. A., Noichl, W., De Marco, F., Frank, M., Urban, T., Schick, R., Gustschin, A., Gleich, B., Herzen, J., Koehler, T., Yaroshenko, A., Pralow, T., Zimmermann, G. S., Renger, B., Sauter, A. P., Pfeiffer, D., Makowski, M. R., Rummeny, E. J., Grenier, P. A., and Pfeiffer, F. (2021). X-ray dark-field chest imaging for detection and quantification of emphysema in patients with chronic obstructive pulmonary disease: a diagnostic accuracy study. *The Lancet Digital Health*, 3(11):e733–e744.

Williams, G. M., Rhee, J., Zou, H., Lee, A., and Ross, S. (2013). Dual threshold X-ray photon counting pixel array detector. In *2013 IEEE Nuclear Science Symposium and Medical Imaging Conference (2013 NSS/MIC)*, pages 1–9. IEEE.

Yang, K., Kwan, A. L. C., Miller, D. F., and Boone, J. M. (2006). A geometric calibration method for cone beam CT systems. *Medical Physics*, 33(6Part1):1695–1706.

Yaroshenko, A., Meinel, F. G., Bech, M., Tapfer, A., Velroyen, A., Schleede, S., Auweter, S., Bohla, A., Yildirim, A., Nikolaou, K., Bamberg, F., Eickelberg, O., Reiser, M. F., and Pfeiffer, F. (2013). Pulmonary emphysema diagnosis with a preclinical small-animal X-ray dark-field scatter-contrast scanner. *Radiology*, 269(2):427–433.

Yoneyama, A., Baba, R., Sumitani, K., and Hirai, Y. (2015). Feasibility study of a high-spatial resolution x-ray computed tomography using sub-pixel shift method. *Applied Physics Letters*, 106(8):084102.

Zdora, M.-C., Thibault, P., Zhou, T., Koch, F. J., Romell, J., Sala, S., Last, A., Rau, C., and Zanette, I. (2017). X-ray Phase-Contrast Imaging and Metrology through Unified Modulated Pattern Analysis. *Physical Review Letters*, 118(20):203903.

Zernike, F. (1942). Phase contrast, a new method for the microscopic observation of transparent objects. *Physica*, 9(7):686–698.

Zhou, T., Zanette, I., Zdora, M.-C., Lundström, U., Larsson, D. H., Hertz, H. M., Pfeiffer, F., and Burvall, A. (2015). Speckle-based x-ray phase-contrast imaging with a laboratory source and the scanning technique. *Optics Letters*, 40(12):2822.

Printed by Media-Tryck, Lund 2023 NORDIC SWAN ECOLABEL 3041 0903

Faculty of Science
Medical Radiation Physics, Lund

ISBN 978-91-8039-613-4